


## Direct numerical simulation of a statistically stationary, turbulent reacting flow

M R Overholt and S B Pope

Sibley School of Mechanical and Aerospace Engineering, Cornell University, Ithaca, NY 14853, USA

Received 21 September 1998, in final form 10 March 1999

**Abstract.** An inhomogeneous, non-premixed, stationary, turbulent, reacting model flow that is accessible to direct numerical simulation (DNS) is described for investigating the effects of mixing on reaction and for testing mixing models. The mixture-fraction–progress-variable approach of Bilger is used, with a model, finite-rate, reversible, single-step thermochemistry, yielding non-trivial stationary solutions corresponding to stable reaction and also allowing local extinction to occur. There is a uniform mean gradient in the mixture fraction, which gives rise to stationarity as well as a flame brush. A range of reaction zone thicknesses and Damkohler numbers are examined, yielding a broad spectrum of behaviour, including thick and thin flames, local extinction and near equilibrium. Based on direct numerical simulations, results from the conditional moment closure (CMC) and the quasi-equilibrium distributed reaction (QEDR) model are evaluated. Large intermittency in the scalar dissipation leads to local extinction in the DNS. In regions of the flow where local extinction is not present, CMC and QEDR based on the local scalar dissipation give good agreement with the DNS.

 This article features multimedia enhancements available from the abstract page in the online journal; see <http://www.iop.org>.

### 1. Introduction

Non-premixed turbulent combustion occurs widely in industry, motivating interest in forming better turbulent combustion models. Since probability density function (PDF) methods treat reaction exactly and thereby show exceptional promise for these flows, a primary interest of the authors is in the development and improvement of PDF mixing models for use in turbulent combustion calculations. Towards this end, direct numerical simulations (DNS) of a new model reacting flow are performed in this work.

In 1989 Givi [1] reviewed the current use of DNS for turbulent reacting flows. Single-step chemistry was used universally at that time. Since then, some research groups have developed multi-step chemistries to address questions such as flame structure and the effects of more detailed chemistry in non-premixed flames [2–4]. All of the references just cited, however, simulate decaying turbulence, which incurs the added difficulties of determining the correct initial conditions and understanding the dependence on the initial condition. There is also the concern that the strong dependence of the Reynolds number on time may mask the phenomena of interest. The more detailed chemistry these groups are implementing is very useful in that it has enabled the investigation of specific questions which single-step chemistries cannot address; however, the price for this capability is high, both in computational cost and in complexity. For these and other reasons we have opted to pursue another track, namely DNS

of stationary, homogeneous, isotropic turbulence with a single-step, model thermochemistry, but one that is finite-rate and reversible, enabling realistic effects such as local extinction and reignition to be predicted qualitatively. A mean mixture-fraction gradient is imposed so that the mixture-fraction variance attains stationarity without forcing, yielding a flame brush. Through an innovative periodic definition of the model thermochemistry we achieve a unique model reacting flow, termed ‘periodic reaction zones’ (PRZ), which is solvable using a Fourier pseudo-spectral method and which incorporates the essential characteristics of non-premixed combustion. This is a fundamentally different approach from that of imposing periodic initial conditions (i.e. slabs of reactants) such as is being utilized by Hill and co-workers [5, 6]. PRZ attains statistical stationarity without any forcing, except as required for the isotropic velocity field, and is very accessible to other numerical methods.

A similar model flow was introduced by Lee and Pope [7]. They performed DNS for stationary, homogeneous, isotropic turbulence, with a single-step, finite-rate, reversible, model thermochemistry implementing the mixture-fraction–progress-variable approach of Bilger [8]. Since they did not have a mean mixture-fraction gradient, the evolution equation for the mixture fraction was modified to include a forcing term to maintain stationarity. They compared DNS results with the predictions of the laminar flamelet model, the conditional moment closure (CMC) model and the quasi-equilibrium distributed reaction (QEDR) model. Results were obtained for a range of reaction zone thicknesses and Damkohler numbers (the ratio of the turbulent mixing time scale to the reaction time scale). They found, as expected, that, at high Damkohler numbers, mixing and reaction balance closely and the models considered performed well. However, as the Damkohler number decreases towards the critical extinction value, mixing begins to overpower reaction resulting in a loss of accuracy of the models. These results were obtained at the low value of the Taylor Reynolds number of 17, however.

This work builds on the results of Lee and Pope [7] by considering a higher Reynolds number, incorporating a mean mixture-fraction gradient and by improving the thermochemistry. A range of reaction zone thicknesses and Damkohler numbers are investigated once again, with a more detailed look at the mechanisms of local extinction in this flow. DNS solutions are then compared with the CMC and QEDR models. For a comparison of these DNS results with Monte Carlo PDF solutions the report by Overholt and Pope [9] should be consulted. A very recent review on DNS of non-premixed turbulent reactive flows is given by Vervisch and Poinso [10].

This paper is organized as follows. Section 2 describes in detail the formulation of the periodic reaction zones model problem, including the model thermochemistry and the boundary conditions, ending with a brief discussion of the CMC and QEDR models. Section 3 describes the DNS simulations, with subsections addressing temporal accuracy, spatial accuracy and the parameter space. This is followed by a section describing the DNS results, with evaluation of the CMC and QEDR models. Finally, section 5 summarizes and gives conclusions.

## **2. Periodic reaction zones**

The complexities of turbulent, reacting flows make it difficult to find accessible model flows for DNS and for testing turbulent reacting flow models. This is especially true for Fourier-based DNS methods which impose spatial periodicity on the flow. The new model flow of Subramaniam [11], termed ‘periodic reaction zones’, shows promise in this regard and is used in this study. This model flow is for constant-density, statistically stationary, isotropic turbulence with a flame brush and a finite-rate, reversible reaction, yet it is periodic and in other ways well suited to DNS.

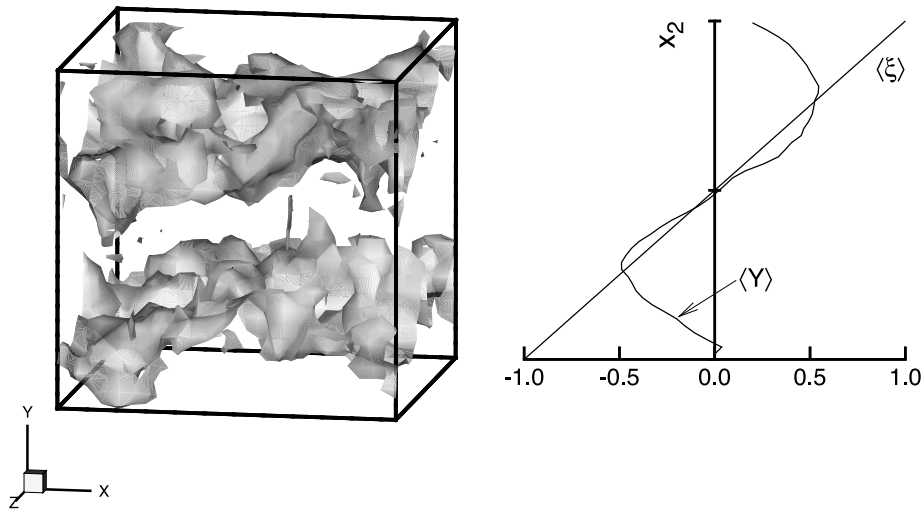


**Figure 1.** DNS solution of PRZ with stoichiometric isosurfaces of  $\xi = -\xi_s = -\frac{1}{2}$  (lower surface) and  $\xi = \xi_s = \frac{1}{2}$  (upper surface), for run 4 at  $t/T_e = 1.42$ . The variation in mean mixture fraction and mean progress variable at this time are shown on the right.

**[M]** An MPEG movie associated with this figure is available from the article's abstract page in the online journal; see <http://www.iop.org>.

Periodic reaction zones is simply a two-scalar formulation for a layered, non-premixed reacting flow, with a constant gradient in the mean mixture fraction producing the layers. The mixture fraction is a conserved scalar, and when it is convected by statistically stationary, homogeneous, isotropic turbulence the result is the often-studied mean scalar-gradient flow [12–16]. What is novel about PRZ is the inclusion of a second scalar, the mass fraction of the product (progress variable) in the finite-rate reaction,



in a manner that provides for the requirements of a statistically stationary, Fourier DNS. These requirements include non-trivial stationary solutions, periodicity and computational tractability. PRZ meets these demands and proves itself useful as well, both for testing turbulence models and for investigating physical phenomena such as local extinction.

Figure 1 illustrates the DNS solution of PRZ, showing the cubical solution domain on the left with isosurfaces of the stoichiometric mixture fractions for the flame and reversed flame. On the right is shown the variation of mean mixture fraction,  $\langle \xi \rangle$ , and mean progress variable,  $\langle Y \rangle$ , in the flow at this time. The layered mixture-fraction field is clearly visible, with large fluctuations in mixture fraction wrinkling the isosurfaces. Fluctuation levels (i.e.  $\xi'$ ) for the other runs are even larger.

To summarize, the PRZ model flow consists of the following elements: a homogeneous, isotropic velocity field, which requires forcing to maintain statistical stationarity; a passive scalar field representing the mixture fraction; and a reacting scalar field representing the perturbation of the progress variable from equilibrium (in place of the progress variable itself, as will be seen). There is a mean gradient in the mixture fraction, enabling it to attain stationarity if the velocity field is stationary. Since the mixture fraction is a passive scalar it is not affected by the reacting scalar. Conversely, the source term in the evolution equation for the reacting

scalar is uniquely determined by the mixture-fraction–progress-variable state. The following subsections address each of these elements in turn.

### 2.1. Velocity field

The velocity field is constant-density, homogeneous, isotropic turbulence, which is forced to maintain statistical stationarity. The deterministic forcing scheme of Overholt and Pope [17] is used, which employs a wavenumber-dependent linear amplification of the lower-wavenumber modes of the three-dimensional (3D) energy spectrum function, relaxing them over time towards a model energy spectrum function, which accurately represents grid turbulence. This forcing scheme was shown to have the significant advantages, over stochastic forcing methods, of not introducing additional statistical variability into the computations and of allowing more physically realistic large-scale motions. In addition, it was advantageous to use this deterministic method in this study because it afforded direct control of both the integral scale,  $\ell$ , and the Kolmogorov scale,  $\eta$ , making it much easier to meet the unique spatial accuracy requirements of each case.

**Table 1.** Results for the DNS runs. Angle brackets  $\langle \rangle$  denote time and volume averaging here.

Parameter		Tabulated	Run 1	Run 2	Run 3	Run 4
$\ell \equiv L_{i,i}/3$	Integral length scale	$\kappa_0 \langle \ell \rangle$	1.75	1.80	1.78	0.672
$\ell_\epsilon \equiv u'^3/\epsilon$	Turbulent length scale	$\langle \ell_\epsilon \rangle / \langle \ell \rangle$	1.03	0.957	0.968	0.943
$\lambda$	Taylor microscale	$\langle \lambda \rangle / \langle \ell \rangle$	0.551	0.521	0.523	0.512
$\eta$	Kolmogorov length scale	$\langle \eta \rangle / \langle \ell \rangle$	0.0517	0.0471	0.0476	0.0492
$T_e$	Eddy turnover time	$\langle \ell / u' \rangle$	2.35	2.22	2.22	0.323
$\tau \equiv k/\epsilon$	Turbulence time scale	$\tau / T_e$	1.54	1.44	1.44	1.46
$\tau_\eta$	Kolmogorov time scale	$\langle \tau_\eta \rangle / T_e$	0.140	0.129	0.129	0.135
$T$	Simulation length	$T / T_e$	1.47	1.49	1.02	3.12
$k$	Turbulent kinetic energy	$\langle k \rangle$	0.840	0.973	0.975	6.13
$u' \equiv (2k/3)^{1/2}$	Turbulence intensity	$u'$	0.748	0.805	0.806	2.02
$\epsilon$	Dissipation rate	$\langle \epsilon \rangle$	0.232	0.303	0.304	13.0
$Re_\ell \equiv u' \ell / \nu$	Reynolds number	$\langle Re_\ell \rangle$	52.8	58.2	57.5	54.5
$Re_\lambda \equiv u' \lambda / \nu$	Taylor Reynolds number	$\langle Re_\lambda \rangle$	29.0	30.3	30.0	27.8
$\rho v \xi$	Mixture-fraction flux correlation	$\langle \rho v \xi \rangle$	−0.716	−0.601	−0.599	−0.600
$\xi'$	Mixture-fraction (rms)	$\langle \phi^2 \rangle^{1/2}$	0.613	0.502	0.512	0.246
$\hat{\xi}_r \equiv \Delta \xi_r / \xi'$	Reaction zone thickness	$\langle \hat{\xi}_r \rangle$	0.757	0.924	0.907	1.88
$\chi$	Scalar dissipation rate	$\langle \chi \rangle$	0.198	0.162	0.156	0.184
$r \equiv 2k/\epsilon / \langle \phi^2 \rangle / \chi$	Time scale ratio	$\langle r \rangle$	1.91	2.08	1.92	1.43
$Da_{\text{crit}}$	Critical Damkohler number	$Da_{\text{crit}}(\langle \hat{\xi}_r \rangle)$	70.5	47.7	49.6	11.4
$Da = \xi'^2 / (\langle \chi \rangle \tau^*)$	Damkohler number	$\langle Da \rangle / Da_{\text{crit}}$	27.4	25.3	52.2	25.2

Characterizations of the velocity field and its response to the various forcing parameters can be found in Overholt and Pope [17]. Table 1 lists a number of field quantities for the four DNS runs ( $\kappa_0$  is the smallest wavenumber, equal to one). The forcing parameters used are listed in table 2 given in section 3.1 in the discussion of the DNS method.

### 2.2. Mixture fraction

This study focuses on the effect mixing has on reaction, and therefore particular importance is placed on the statistics of the passive scalar, the mixture fraction.

The mixture fraction is defined as in Bilger [18]:

$$\xi \equiv \frac{\varphi - \varphi_O}{\varphi_F - \varphi_O} \quad (2)$$

where  $\varphi$  is a conserved scalar (Shvab–Zeldovich function) formed by the appropriate linear combinations of the mass fractions of the three species (fuel, oxidizer and product),  $\varphi_O$  is a constant equal to the value of  $\varphi$  in pure oxidizer and  $\varphi_F$  is a constant equal to the value of  $\varphi$  in pure fuel. Hence the mixture fraction is a conserved scalar equal to one in pure fuel and zero in pure oxidizer.

The mixture fraction evolves by the convection–diffusion equation,

$$\frac{\partial \xi}{\partial t} + U_j \frac{\partial \xi}{\partial x_j} = \Gamma \frac{\partial^2 \xi}{\partial x_j \partial x_j} \quad (3)$$

where  $\Gamma$  is the molecular diffusivity, taken to be constant. As in Overholt and Pope [16], the uniform mean mixture-fraction gradient  $\beta$  is imposed in the  $x_2$ -direction on the statistically homogeneous mixture-fraction fluctuation field  $\phi$ , yielding an inhomogeneous mixture-fraction field. Reynolds decomposing into mean and fluctuating parts, then, as

$$\xi = \langle \xi \rangle + \phi \quad (4)$$

$$U_i = \langle U_i \rangle + u_i \quad (5)$$

with appropriate conditions

$$\frac{\partial \langle \xi \rangle}{\partial x_j} = \beta \delta_{j2} \quad (6)$$

$$\langle U_i \rangle = 0 \quad (7)$$

yields the stationary, mean scalar-variance evolution equation for this study

$$\frac{d}{dt} \langle \phi^2 \rangle = -2 \langle u_2 \phi \rangle \beta - \langle \chi \rangle \quad (8)$$

where the scalar dissipation is defined as

$$\chi \equiv 2\Gamma \left( \frac{\partial \phi}{\partial x_j} \frac{\partial \phi}{\partial x_j} \right). \quad (9)$$

Numerous passive scalar studies of this flow have been performed, theoretically [19–21], experimentally [22–28] and numerically [12–16, 29, 30]. Most notably, the statistics reported by Overholt and Pope [16] correspond directly to those of the mixture-fraction fluctuation,  $\phi(\mathbf{x}, t)$ , in this study. They used the stochastic forcing of Eswaran and Pope [31]; however, as was shown in Overholt and Pope [17], the deterministic forcing scheme used for this study yields the same mean statistics, but with reduced variability.

The passive scalar study of Overholt and Pope [16] used a value of  $\beta$  three times larger than that used in this study. However, since the evolution equation for  $\phi$  is linear in  $\beta$ , the statistics of  $\phi/\beta$  are independent of  $\beta$ . Therefore, the passive scalar study of Overholt and Pope [16] provides appropriate mixture-fraction fluctuation statistics for this study, and a proper basis for the current investigation of the effects of mixing on reaction.

Among the most significant findings of that work as it relates to this study are the following: the one-point PDF of  $\phi$  is Gaussian and the statistics of both dissipation and scalar dissipation are stretched exponentials. A number of other time- and volume-averaged mixture-fraction statistics are given in table 1 for the four DNS runs of this study.

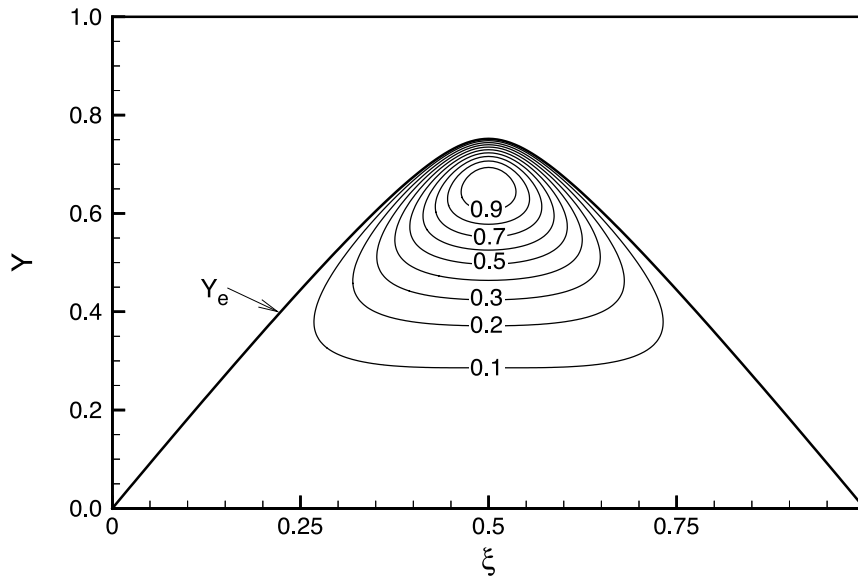


**Figure 2.** Contours of the normalized reaction rate  $S(\xi, Y)\tau_c/\Delta\xi_e$ . The reaction zone width,  $\Delta\xi_r = 0.464$ , is taken to be the maximum width in  $\xi$  of the 0.10 contour line.

### 2.3. Progress variable and thermochemistry

Following Bilger's formulation [8, 18, 32], the second scalar is taken to be the mass fraction of product,  $Y$ , and is called the 'reaction progress variable'. It evolves by the equation

$$\frac{\partial Y}{\partial t} + U_j \frac{\partial Y}{\partial x_j} = \Gamma \frac{\partial^2 Y}{\partial x_j \partial x_j} + S \quad (10)$$

where the molecular diffusivity,  $\Gamma$ , is the same as that for the mixture fraction, and  $S$  is the model reaction rate source term, uniquely determined by the  $\xi$ - $Y$  state. The reaction rate is shown in figure 2, normalized by the chemical time scale  $\tau_c$  and the characteristic length scale in  $\xi$ -space of the reaction rate,  $\Delta\xi_e$  (a measure of the width of the curved portion of  $Y_e$  around  $\xi_s$ ). For a given  $\xi$ , the realizable values of  $Y$  are  $[0, Y_e(\xi)]$ , where  $Y_e(\xi)$  is the equilibrium value (where forward and reverse reaction rates in equation (1) balance). The stoichiometric value  $\xi_s$  is taken to be  $\frac{1}{2}$ . The figure gives the reaction zone width,  $\Delta\xi_r$ , which is a useful quantity in discussions of flame thickness (see section 3.3) and directly related to  $\Delta\xi_e$ . Details of the thermochemistry formulation can be found in the appendix.

In the previous section the convection-diffusion equation was shown to govern the evolution of the mixture fraction. Although the mixture fraction has a physical meaning only in the interval  $[0, 1]$ , its evolution equation allows it to take on any value. The only way to avoid this difficulty would be to solve equations for two reacting scalars, say the fuel and oxidizer mass fractions, and then define the mixture fraction based on those two variables. However, such an approach entails the need for two reaction rate source terms, which is not desirable. Therefore, it is necessary to extend the thermochemistry definition to allow for all values of mixture fraction.

Subramaniam [11] showed that the correct way to extend this thermochemistry is as plotted in figure 3, or more specifically,

$$Y_e(\xi) = Y_e(\xi - [\xi]) \quad \xi \in [2n, 2n + 1] \quad (11)$$

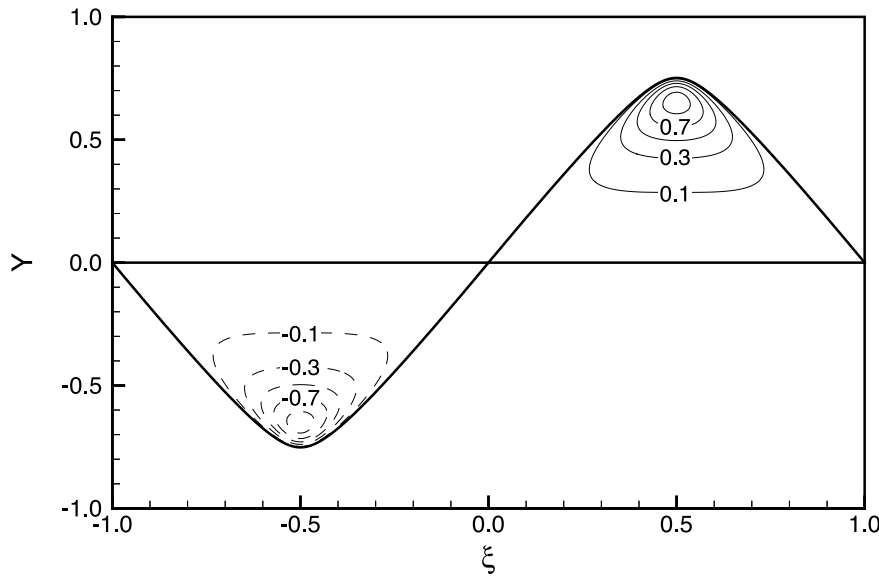


Figure 3. Periodic extension of the normalized reaction rate,  $S(\xi, Y)\tau_c/\Delta\xi_e$ .

$$Y_e(\xi) = -Y_e([\xi] - \xi) \quad \xi \in [2n - 1, 2n] \quad (12)$$

$$S(\xi, Y) = S(\xi - [\xi], Y) \quad \xi \in [2n, 2n + 1] \quad (13)$$

$$S(\xi, Y) = -S([\xi] - \xi, Y) \quad \xi \in [2n - 1, 2n] \quad (14)$$

where  $[\xi]$  is the smallest integer larger than  $\xi$ ,  $[\xi]$  is the largest integer smaller than  $\xi$  and  $n$  is any integer. Both  $Y_e$  and  $S$  are periodic in  $\xi$ , and are antisymmetric about the origin. The period, denoted by  $\Delta\xi_L$ , is 2. Each period is composed of a positive portion and a negative portion. The negative portions not only have  $Y \leq 0$ , but  $S \leq 0$  as well. This means that realizable regions where  $Y$  is positive and less than  $Y_e$ , the equilibrium value, are effecting a net creation of product, while the realizable negative regions where  $Y$  is greater than  $Y_e$  are effecting a net creation of reactants. Therefore, with mixing between the positive and negative regions, stationary solutions are possible at values of  $Y$  other than  $Y_e$  and zero, which is highly desirable. Although the negative regions appear to be non-physical, they are well motivated mathematically and can be interpreted in physical terms. In particular, the statistics of  $([\xi] - \xi, -Y)$  in 'reversed flames' are identical to those of  $(\xi, Y)$  in 'flames'.

In order to facilitate future discussions it is useful to introduce the following definitions. The positive regions spoken of in the preceding paragraph are called 'flames' and the negative regions 'reversed flames'. Similarly, we denote as 'flame zones' the reactive regions  $\xi_{RF}$ ,

$$\xi_{RF} \equiv [\xi_s + 2n - \frac{1}{2}\Delta\xi_r, \xi_s + 2n + \frac{1}{2}\Delta\xi_r] \quad (15)$$

for any integer  $n$ , and as 'reversed zones' the reactive regions  $\xi_{RR}$ ,

$$\xi_{RR} \equiv [\xi_s + 2n + 1 - \frac{1}{2}\Delta\xi_r, \xi_s + 2n + 1 + \frac{1}{2}\Delta\xi_r] \quad (16)$$

where  $\xi_s$  is the stoichiometric value of the mixture fraction. Finally, we use the term 'reaction zones', or  $\xi_R$ , to denote the sum of the above,

$$\xi_R \equiv [\xi_s + n - \frac{1}{2}\Delta\xi_r, \xi_s + n + \frac{1}{2}\Delta\xi_r]. \quad (17)$$

It is also useful to define the perturbation of the reaction progress variable from equilibrium,

$$y(\mathbf{x}, t) \equiv Y_e[\xi(\mathbf{x}, t)] - Y(\mathbf{x}, t). \quad (18)$$

For very high reaction rates (high Damkohler number), the reaction is stable and the stationary solution for  $Y$  approaches  $Y_e$ . Since  $Y_e$  is a function of the mixture fraction (which is statistically inhomogeneous in the  $x_2$ -direction), it is often more instructive to examine the statistics of the progress-variable perturbation instead of the progress variable itself. The governing equation for the perturbation is derived by substituting equation (18) into equation (10) and using equations (3), (5), (7) and continuity, which yields

$$\frac{\partial y}{\partial t} + \frac{\partial(u_j y)}{\partial x_j} = \Gamma \frac{\partial^2 y}{\partial x_j \partial x_j} - \Gamma \left( \frac{\partial \xi}{\partial x_j} \frac{\partial \xi}{\partial x_j} \right) Y_e'' - S \quad (19)$$

where  $Y_e''$  is the second derivative of the equilibrium function with respect to  $\xi$ . Since the scalar fields are homogeneous in every spatial direction except for  $x_2$ , taking expectations results in the equation

$$\frac{\partial \langle y \rangle}{\partial t} + \frac{\partial \langle u_2 y \rangle}{\partial x_2} = \Gamma \frac{\partial^2 \langle y \rangle}{\partial x_j \partial x_j} - \Gamma \left\langle \frac{\partial \xi}{\partial x_j} \frac{\partial \xi}{\partial x_j} Y_e'' \right\rangle - \langle S \rangle. \quad (20)$$

The terms in this equation are, from left to right, the change in  $\langle y \rangle$ , turbulent transport, molecular transport, microscale mixing and reaction rate. As has been shown by Lee and Pope [7], the microscale mixing and reaction rate terms are always as large as the largest terms in this equation, balancing each other at equilibrium. Additionally, at a sufficiently high Damkohler number the two transport terms are negligible.

With  $\xi_s = \frac{1}{2}$ , the time-dependent surfaces defined by  $\xi(\mathbf{x}, t) = 2n + \frac{1}{2}$  are the stoichiometric surfaces of the flames, and similarly,  $\xi(\mathbf{x}, t) = 2n - \frac{1}{2}$  are the stoichiometric surfaces of the reversed flames. The surfaces  $\xi(\mathbf{x}, t) = n$  are the interfaces between the flames and the reversed flames and correspond to pure reactants. Accordingly, the boundary condition  $Y = 0$  is imposed on these surfaces, i.e.

$$Y(\mathbf{x}, t) = 0 \quad \text{for } \mathbf{x} \text{ such that } \xi(\mathbf{x}, t) = n. \quad (21)$$

In section 3.1 numerical issues arising in the implementation of these boundary conditions are addressed.

In summary, the second scalar adds the following parameters to the flow: a time scale for the reaction,  $\tau^*$ ; a reaction zone width,  $\Delta \xi_r$  (or alternatively, the length scale,  $\Delta \xi_e$ ); and a periodicity in  $\xi$ ,  $\Delta \xi_L$ . Therefore, PRZ can be characterized by three non-dimensional parameters: the Reynolds number, a Damkohler number ratio ( $Da/Da_{crit}$ ) and a reaction zone thickness parameter, defined as  $\hat{\xi}_r \equiv \Delta \xi_r / \xi'$ , where  $\xi'$  is the rms mixture-fraction fluctuation. Further discussion of the parameter space is postponed until section 3.3.

#### 2.4. Simple models: CMC and QEDR

The CMC, developed by Bilger [18] (similar to that derived independently by Klimenko [33]), is based on the hypothesis that the fluctuations in  $Y$  arise primarily from fluctuations in  $\xi$ . Using this assumption an evolution equation can be derived for the conditional mean of  $Y$ , a single and tractable ODE. This is a first-moment or average closure; higher-order closures for the conditional reaction rate are possible and even recommended for flows with local extinction [34–38]. However, higher-order closures are not considered in this study, and all further use of the term ‘CMC’ refers to the first-moment CMC. For details on the solution of



CMC see Overholt and Pope [9]. CMC predicts stable combustion above a critical value of the Damkohler number,  $Da_{\text{crit}}$ , and extinction for  $Da < Da_{\text{crit}}$ . In table 1 the critical  $Da$  as determined from CMC,  $Da_{\text{crit}}$ , is given. Then, in section 4.3, CMC solutions for conditional  $y$  are compared with the DNS results.

The QEDR model [39] assumes high  $Da$  such that the microscale mixing and reaction rate terms in equation (19) balance each other. The other terms are taken to be negligible. Hence the spatial structure of the reaction zone is determinable from the spatial structure of the mixing field. Given an expression for the reaction rate, this approximation results in a simple algebraic equation for  $y$ . Details are given in Overholt and Pope [9]. QEDR predictions are compared with CMC and DNS results in the next section.

### 3. Direct numerical simulations

#### 3.1. Pseudo-spectral method

The DNS algorithm is based on the pseudo-spectral method of Rogallo [40], and uses the same fully parallelized code as was used in Overholt and Pope [16] with the new deterministic forcing scheme presented in Overholt and Pope [17]. The full, incompressible Navier–Stokes equations and evolution equations for  $\xi$  and  $y$  are solved on a three-dimensional grid. The grid is a cube with sides of length  $2\pi$  in physical space, resulting in integer wavenumbers. An explicit, second-order Runge–Kutta method advances the solution in time steps  $\Delta t$ .

Aliasing errors incurred in the discrete fast Fourier transforms (FFTs) are reduced by a combination of phase shifting and truncation techniques, which have been shown to almost completely remove the aliasing error due to the quadratic nonlinearities of the convection terms [40]. However, the evolution equation for  $y$  contains several additional terms with higher-order nonlinearities which must be carefully treated to ensure that aliasing error is not incurred [7] (addressed in section 3.2). The truncation for aliasing error removal results in a maximum significant wavenumber of  $\kappa_{\text{max}} = \sqrt{2}N\kappa_0/3$ , where  $N$  is the number of grid points in each direction.

The deterministic forcing method requires the input of several parameters which define the target model energy spectrum function and the number of modes forced [17]. Table 2 gives values for these and other parameters for the simulations in this work.

To maintain realizability, the boundary condition given by equation (21) is enforced for  $\xi(\mathbf{x}, t) \in (n + a, n - a)$ , where  $a \ll 1$ . Given completely accurate numerics, there should be no realizability violations. If, however, small realizability violations occur due to numerical error, they are corrected (e.g. if  $Y(\xi)$  becomes slightly greater than  $Y_e(\xi)$ , then the value of  $Y(\xi)$  is reset to  $Y_e(\xi)$  and the reaction rate set to zero).

**Table 2.** Run input parameters.

Parameter		Run 1	Run 2	Run 3	Run 4
$N$	Grid size	160	128	128	192
$\nu$	Kinematic viscosity	0.025	0.025	0.025	0.025
$Pr$	Prandtl number	0.7	0.7	0.7	0.7
$\beta$	Mean scalar gradient	$1/\pi$	$1/\pi$	$1/\pi$	$1/\pi$
$E_L^*$	% energy captured	0.75	0.79	0.79	0.99
$E_f^*$	% energy forced	0.80	0.80	0.80	0.85
$\kappa_\eta^*$	$\kappa_{\text{max}}\eta$ desired	4.945	3.636	3.636	2.086
$\tau^*/\langle\tau_\eta\rangle$	Chemical time scale	$3.04 \times 10^{-3}$	$4.52 \times 10^{-3}$	$2.26 \times 10^{-3}$	$2.73 \times 10^{-2}$
$\Delta t/\tau^*$	Time step ratio	0.2	0.2	0.2	0.2

### 3.2. Accuracy

It has been well established that temporal accuracy of the velocity fields is obtained if the time step  $\Delta t_u$  results in a Courant number  $C \leq 1$  [31]; however, the perturbation  $y$  evolves by the chemical time scale  $\tau^*$ , which is entirely independent of  $\Delta t_u$ . In order to march all the fields with the same time step,  $\Delta t$ , that time step must be defined such that

$$\max\{\Delta t\} = \min\{\Delta t_u, \Delta t_y\} \quad (22)$$

where  $\Delta t_y$  is related to  $\tau^*$  in some as yet unknown manner. In the related work by Lee and Pope [7], they found it sufficient to use

$$\Delta t_y < \tau^*. \quad (23)$$

However, in that study the scalar variance was forced, whereas in this one it is not. For this and other reasons temporal accuracy was re-examined for these simulations using the following methodology. First, for a given grid size a very well resolved initial condition was obtained. Then, short runs of a fixed time duration, less than an eddy-turnover time, were made using different values of  $\Delta t/\tau^*$ . At the end of the run, the  $y$ -fields were compared directly in physical space (i.e. grid point by grid point) with the solution obtained for the smallest time step ( $\Delta t/\tau^* = 0.10$ ). This was performed for three different flows, all at high  $Da$ , and the maximum and average differences were compared with the reference value for  $y$ . This reference value,  $y_{\text{ref}}$ , results from the high  $Da$  approximation

$$\frac{y}{\tau^*} \approx -\Gamma(\nabla\xi \cdot \nabla\xi) Y_e''(\xi). \quad (24)$$

At the stoichiometric value of  $\xi$ ,  $\xi_s$ , where  $|Y_e''|$  is the largest, the additional approximation

$$\Gamma(\nabla\xi \cdot \nabla\xi) \approx \Gamma\beta^2 + \frac{1}{2}\langle\chi\rangle$$

yields

$$y_{\text{ref}} = (\Gamma\beta^2 + \frac{1}{2}\langle\chi\rangle) |Y_e''(\xi_s)|\tau^*. \quad (25)$$

The results clearly show that equation (23) is sufficient to ensure second-order accuracy, as expected for our time-stepping scheme; however, in order to maintain a maximum difference of an order of magnitude less than the reference value, a maximum time step of  $0.4\tau^*$  is required. To ensure good accuracy we use

$$\Delta t_y = \frac{1}{5}\tau^*. \quad (26)$$

Regarding spatial accuracy, Lee and Pope [7] made a careful study of the spatial accuracy requirements for the reacting scalar, resulting in several observations. They began by noting that the microscale mixing and reaction rate terms are always dominant, or at least as large as the largest terms in the evolution equation for  $y$ , leading to their conclusion that, if the microscale mixing term was adequately resolved, then the reaction rate term would also be well resolved. Under this assumption they proceeded to study the spatial accuracy requirements for microscale mixing and found that, for Taylor Reynolds numbers in the range [18, 100], the empirical relation

$$\kappa_{\text{max}}\eta \geq \frac{6.2}{\hat{\xi}_t} + 1.1 \quad (27)$$

assured good accuracy. Obviously, this condition always gives good resolution of the velocity and passive scalar fields as well.

There are several differences between Lee and Pope's work [7] and this study, one being the difference in chemistry. The reaction rate length scale,  $\Delta\xi_e$ , is taken to be twice as large as that used by Lee and Pope [7] in the hope that the factor 6.2 in equation (27) would scale linearly with  $1/\Delta\xi_e$ , i.e. that

$$\kappa_{\max}\eta \geq \frac{0.20}{\hat{\xi}_r\Delta\xi_e} + 1.1 \quad (28)$$

would hold. In order to test this condition the spatial accuracy requirements for  $y$  were tested again in this work, using an approach similar to that used for temporal accuracy, except that in this case the grid sizes were varied from  $32^3$  to  $128^3$ , with the common nodes being compared to the  $128^3$  solution. A time step of  $\Delta t = 0.1\tau^*$  was used. The results show that satisfaction of equation (28) results in maximum differences of more than an order of magnitude less than the reference value, which we took as sufficient evidence to use this scaled accuracy requirement with confidence for this PRZ model flow.

### 3.3. Choice of parameters

As introduced in section 2.3, PRZ is characterized by a Reynolds number, a Damkohler number, and a non-dimensional reaction zone thickness,  $\hat{\xi}_r = \Delta\xi_r/\xi'$ . In this section the  $Re-Da-\hat{\xi}_r$  parameter space is discussed, showing the rationale for the runs chosen for this study. The following subsection discusses the choice of the parameters defining the chemistry.

Unlike the case with premixed reacting flows, characteristic regions of behaviour for non-premixed reacting flows are not well established. We simply make distinctions of flame thickness and of reaction rate. Flame thickness distinctions are based on the reaction zone thickness parameter,  $\hat{\xi}_r$ , where values greater than one are taken to be 'thick flames' and values of less than one 'thin flames'. Thick flames correspond to mixture-fraction fluctuations smaller than the reaction zone width,  $\Delta\xi_r$ , and narrow flame brushes (the width in the  $x_2$ -direction swept out by the fluctuating stoichiometric isosurface). Conversely, thin flames correspond to mixture-fraction fluctuations larger than  $\Delta\xi_r$ , giving wide flame brushes.

The reaction rate is well characterized by  $Da$ . Additionally,  $Da$  is divided by the critical value predicted by CMC for global extinction,  $Da_{\text{crit}}$ , yielding the Damkohler number ratio referred to previously. This gives a measure of how far the flow is from global extinction (assuming, for the purposes of this study, that the DNS solution will experience global extinction at the same value as that predicted by CMC), which is of particular practical importance since models based on near-equilibrium assumptions, such as QEDR, are known to break down when the flow nears extinction.

In choosing the parameter space to be investigated by the four runs in this study, we began by deciding to fix the Reynolds number at the largest value that could be simulated given a reasonably wide range of  $\hat{\xi}_r$  (to be chosen) and constraints of time and computational cost ( $Re_\lambda \approx 30$ ). Three of the runs were then chosen to span the greatest possible width in  $\hat{\xi}_r$ -space at a fixed  $Da$  ratio, with the fourth run duplicating one of the first three at a higher  $Da$  (see table 1). The two  $Da$ -ratio values were chosen somewhat arbitrarily to be 25 and 50, with the goal of seeing local extinction (but not global extinction) at 25 and very little local extinction at 50.

**3.3.1. Chemistry.** The chemistry formulation described in the appendix has several variable parameters, the choices of which are discussed in this section. For DNS it is advantageous to have as large a physical length scale,  $\Delta\xi_e$ , as possible, since that directly affects the spatial accuracy requirements. Lee used a value of  $\Delta\xi_e$  of 0.0318, which corresponds to a value of

$|Y_e''|_{\max}$  of 40. As seen in the appendix, the chemistry is defined for any non-zero value of  $|Y_e''|_{\max}$ , but for values less than about 20 the reaction rate function,  $S$ , loses its resemblance to real combustion systems. Hence a value of  $|Y_e''|_{\max}$  of 20 was chosen for this study, giving a value of  $\Delta\xi_e$  of 0.0637.

There are two other parameters which must be chosen in order to define the chemistry, the constants  $C$  and  $B$  (see equations (A.10) and (A.11)). Parameter  $C$  determines the ratio  $\Delta\xi_e/\Delta\xi_r$ . A value of  $C$  of 0.529 was chosen to match that of Lee and Pope [11], which, given a value of  $\Delta\xi_e$  of 0.0637, results in a reaction zone width  $\Delta\xi_r$  of 0.464. The actual value of  $\Delta\xi_r$  is important for DNS, due to its influence on the reaction zone thickness parameter  $\hat{\xi}_r = \Delta\xi_r/\xi'$ . The scalar rms,  $\xi'$ , scales like  $\beta l_\epsilon$ , and  $l_\epsilon$  has a limited range of practical values. Therefore, it is important to choose a good value for  $\Delta\xi_r$  such that  $l_\epsilon$  can be as large as possible for the desired  $\hat{\xi}_r$ , thereby maximizing the Reynolds number.

This leaves  $B$  to be determined such that the function  $f(y)$  is negligible at  $y = Y_e$  (or  $Y = 0$ ). Using the arbitrary criterion of requiring  $f(Y_e) < 0.01 \max(f)$  results in a total error in  $S$  of  $1.6 \times 10^{-5}$  at integer values of  $\xi$ , and a value of  $B$  of  $10.5\Delta\xi_e = 0.668$ . The resulting reaction rate is that shown in figure 2.

#### 4. DNS results

As seen in the previous section, there is considerable computational cost involved in fully resolving this flow. Hence the DNS simulations represented in table 1 are for simply one realization and relatively short periods of time. Therefore, the results are subject to the variability inherent in DNS, as discussed at length in Lee and Pope [7] and evident in figure 4. For this reason the approach taken was to examine simulation details (e.g. individual fields undergoing local extinction) rather than to present global statistics such as the critical  $Da$ , which would be rendered useless due to the resulting large confidence intervals. In fact, the issue of global statistics is further complicated in this flow by the spatial variation in the  $x_2$ -

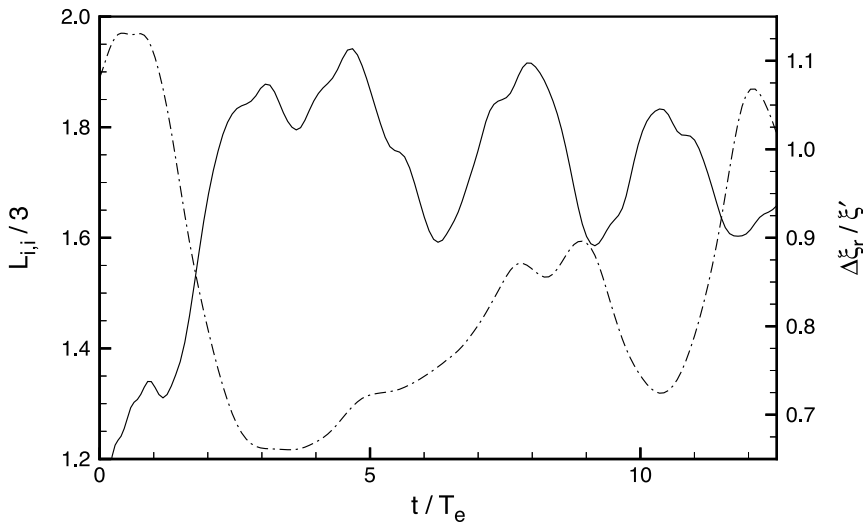


**Figure 4.** Fluctuations of volume-averaged quantities in the velocity and mixture-fraction fields: —,  $L_{i,i}/3$ ; - - -,  $\hat{\xi}_r$ . Run 1 was taken from the portion  $t/T_e = [9.35, 10.85]$ .

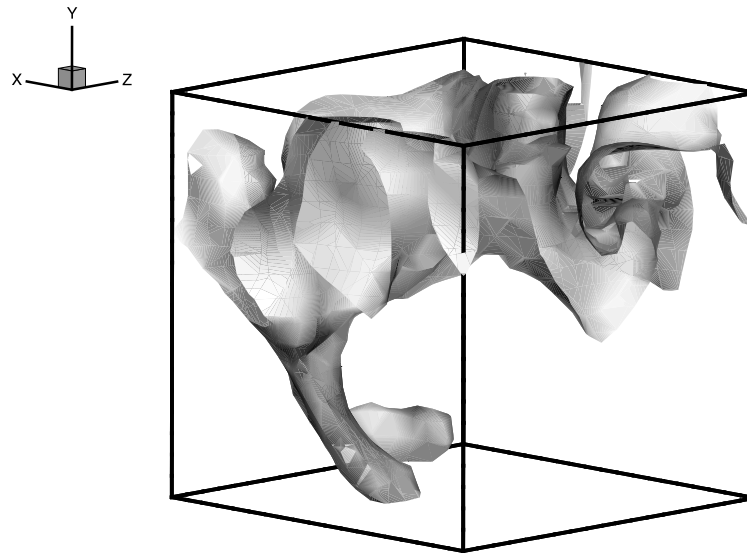


Figure 5. Stoichiometric isosurface of  $\xi = \xi_s$  for run 1 at  $t/T_e = 1.41$ .

direction, implying that conditioning will be required. We leave the gathering of such statistics to future work.

#### 4.1. Characterization of the flame brush

One of the two flow parameters varied is the reaction zone width,  $\hat{\xi}_r$ , which depends inversely on the rms mixture fraction. The flame brush, defined as the area swept out in the  $x_2$ -direction by the stoichiometric mixture-fraction isosurface, characterizes the mixture-fraction fluctuations. Figures 1 and 5 show the instantaneous, stoichiometric, mixture-fraction isosurface(s) for runs 4 and 1 and illustrate the differing fluctuations levels  $\xi'$  at the extremes of  $\hat{\xi}_r$  examined. The isosurface in the second figure has several notable features. First of all, on the right-hand side it is intricately coiled up around itself. On the left-hand side a slab-like finger is jutting far into the lower portion of the domain. Such features are relatively common in these simulations. (Note for the electronic version: an MPEG movie of the evolution of the stoichiometric isosurfaces is available.)

Scatter plots of  $\xi$  versus  $x_2/L$  are shown in figures 6 and 7, where the flame brush can be interpreted as the extent of the fluctuations along the line  $\xi = 0.5$ . Each figure consists of about 5000 samples taken from a regularly spaced grid. The spatial variations visible in the scatter plots for the first run, run 1, are due to the large size of the integral scales (relative to the computational domain) yielding many fewer of the largest eddies for statistical averaging purposes than are present in the last run. The larger fluctuations present in the first run are also apparent. In run 1 the flame brush traverses over three-quarters of the domain, producing extensive wrinkling of the isosurface and area ratios (to be defined) in excess of five. Runs 2 and 3 are very similar to run 1, due to their similar values of  $\hat{\xi}_r$ .

Although more common in discussions of premixed flames, the surface-to-volume and area ratios give another measure of the mixture-fraction fluctuations in these runs. The surface-to-volume ratio of the constant property surface (or isosurface)  $\xi = \Psi$  is found using the relation

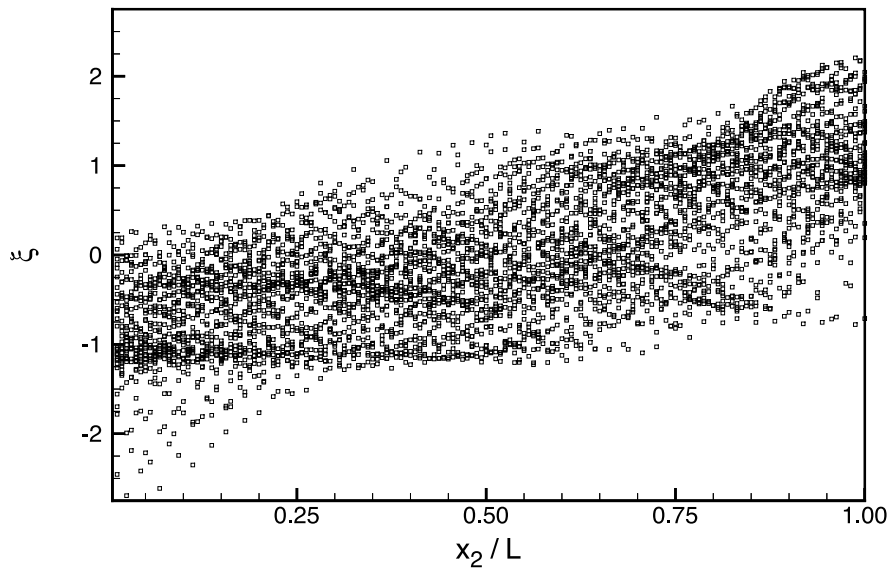


Figure 6. Scatter plot of mixture fraction versus  $x_2/L$  for run 1 at time  $t/T_e = 0.26$  (5001 points).

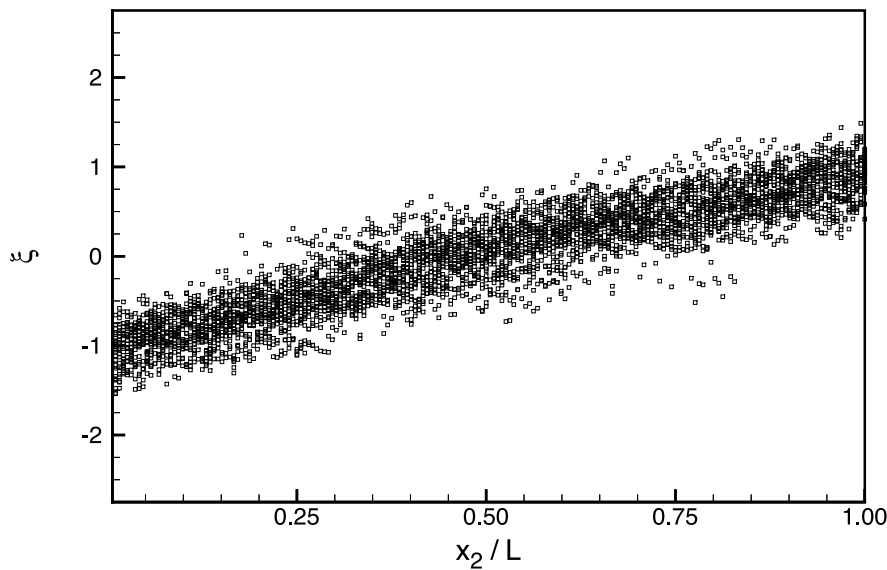


Figure 7. Scatter plot of mixture fraction versus  $x_2/L$  for run 4 at time  $t/T_e = 0.39$  (5002 points).

of Pope [41]

$$\Sigma(x_2; \Psi) = f_{\xi}(x_2; \Psi) \langle |\nabla \xi| | \xi = \Psi \rangle \tag{29}$$

where  $f_{\xi}(x_2; \Psi)$  is the PDF of the mixture fraction. The area ratio of that surface can be found, then, as the integral

$$\frac{A}{L^2} = \int_0^L f_{\xi}(x_2; \Psi) \langle |\nabla \xi| | \xi = \Psi \rangle dx_2. \tag{30}$$

In the work of Overholt and Pope [16] it was found that the PDF of  $\phi$  is Gaussian at this Reynolds number, and that the conditional  $\langle \chi | \phi = \psi \rangle$  is equal to the unconditional  $\langle \chi \rangle$ . If, in addition,  $\nabla \xi \cdot \nabla \xi$  is taken to be log-normal, it can be shown that

$$\langle |\nabla \xi| \rangle = \langle \nabla \xi \cdot \nabla \xi \rangle^{1/2} e^{-\sigma^2/8} \quad (31)$$

where

$$\sigma^2 = \text{var}[\ln(\chi)].$$

Making use of these two approximations and the time-averaged values of  $\text{var}[\ln(\chi)]$  (see table 3),  $\Sigma$  can be predicted, yielding results very close to those calculated by the DNS.

**Table 3.** Average moments for the PDF  $f_{\ln(\chi^*)}$ .

Moment	Run 1	Run 2	Run 4
Mean	-0.90	-1.19	-1.08
Variance	2.15	2.20	2.34
Skewness	-0.128	-0.003	-0.044
Kurtosis	2.97	3.07	2.97
Superskewness	16.5	17.3	15.9

Figure 8 compares the time-averaged DNS results (symbols) for  $\Sigma(x_2; \xi_s)$  versus the mean mixture fraction ( $\langle \xi \rangle(x_2) = \Delta \xi_L(x_2/L - \frac{1}{2})$ ) for each of the runs to that predicted by equation (31) (curves), with the corresponding area ratios given in the caption. Note that, due to periodicity, the right-hand side tails of the  $\Sigma$  plots extend into the left-hand side (since the stoichiometric surface of  $\xi = -\frac{3}{2}$  is simply a periodic extension of the  $\xi = \frac{1}{2}$  surface). All the runs had average area ratios greater than five, which is double that usually seen in the literature, and the predicted integrated area ratios are within 8% of those calculated by the DNS.

#### 4.2. Statistical variation

In addition to the statistical variations inherent in DNS and mentioned earlier, there are very large spatial variations in the instantaneous scalar dissipation fields. It was found that the reacting scalar results were strongly dependent on these statistical variations of  $\chi$ ; therefore, discussions of  $y$  are prefaced here by an investigation of  $\chi$ . For normalization purposes a nominal value of  $\langle \chi \rangle_{\text{ref}} = 0.18$  is used (the mean value of  $\chi$  for all the runs, see table 1). The corresponding reference  $y$  value, as defined by equation (25), is tabulated in table 4. Using this  $y_{\text{ref}}$  the normalized variable  $y^*$  is defined as

$$y^* \equiv \left| \frac{y}{y_{\text{ref}}} \right|. \quad (32)$$

The large variations in  $\chi$  can be seen in figure 9, which shows a contour plot of  $\log_{10}(\chi^*/\chi_q^*)$ , where

$$\chi^* \equiv \frac{\chi}{\langle \chi \rangle_{\text{ref}}}.$$

Based on the values of  $Da_{\text{crit}}$  from CMC and of the mean  $\langle \xi'^2 \rangle$ , both given in table 1, a normalized, critical value of scalar dissipation can be defined as

$$\chi_q^* \equiv \frac{\langle \xi'^2 \rangle}{\tau^* \langle \chi \rangle_{\text{ref}} Da_{\text{crit}}}. \quad (33)$$

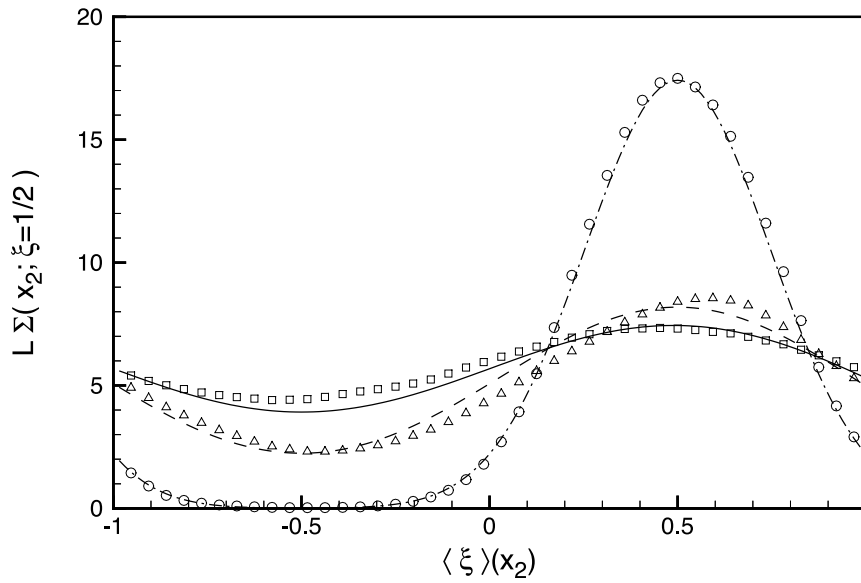


**Figure 8.** Normalized surface-to-volume ratios for  $\xi = \xi_s$ , time-averaged over the entire run. DNS:  $\square$ , run 1,  $A/L^2 = 5.86$ ;  $\triangle$ , run 2,  $A/L^2 = 5.10$ ;  $\circ$ , run 4,  $A/L^2 = 5.53$ . Predicted: —, run 1,  $A/L^2 = 5.40$ ; - - -, run 2,  $A/L^2 = 5.14$ ; - · -, run 4,  $A/L^2 = 5.65$ .

**Table 4.** Reference  $y$  value.

Parameter	Run 1	Run 2	Run 3	Run 4
$y_{\text{ref}}$ Reference $y$ value	$1.87 \times 10^{-3}$	$2.43 \times 10^{-3}$	$1.22 \times 10^{-3}$	$2.24 \times 10^{-3}$

**Table 5.** Normalized critical value of scalar dissipation.

Parameter	Run 1	Run 2	Run 3	Run 4
$\chi_q^*$ Critical value of $\chi/\langle\chi\rangle_{\text{ref}}$	29.6	22.6	45.1	24.7

The critical values for each run are listed in table 5.

In figure 9 contours are only shown for the largest values of  $\chi^*/\chi_q^*$ , since they appear to be the most significant factor in triggering local extinction, as will be seen. (The contour values shown are for the logged ratio  $\chi^*/\chi_q^*$ , and since  $\chi^*$  rarely exceeds  $\chi_q^*$ , the highest values of the logged ratio are near zero and negative.) Note that the very highest levels ( $-0.3$ , full) are on the stoichiometric isosurface in the reversed zone. It is not clear, however, why there appears to be a clustering of high values of  $\chi$  around the stoichiometric surfaces, since the  $\phi$  field is statistically homogeneous. The large extent of the scalar dissipation fluctuations is an intermittency effect, which is clearly present even at the moderate Reynolds number of these simulations.

The very large range of  $\chi$ -fluctuations is most clearly shown in its PDF in figure 10,  $f_{\chi^*}(X^*; t)$ , where  $X$  is the sample-space variable for  $\chi$  and

$$X^* \equiv \frac{X}{\langle\chi\rangle_{\text{ref}}}.$$



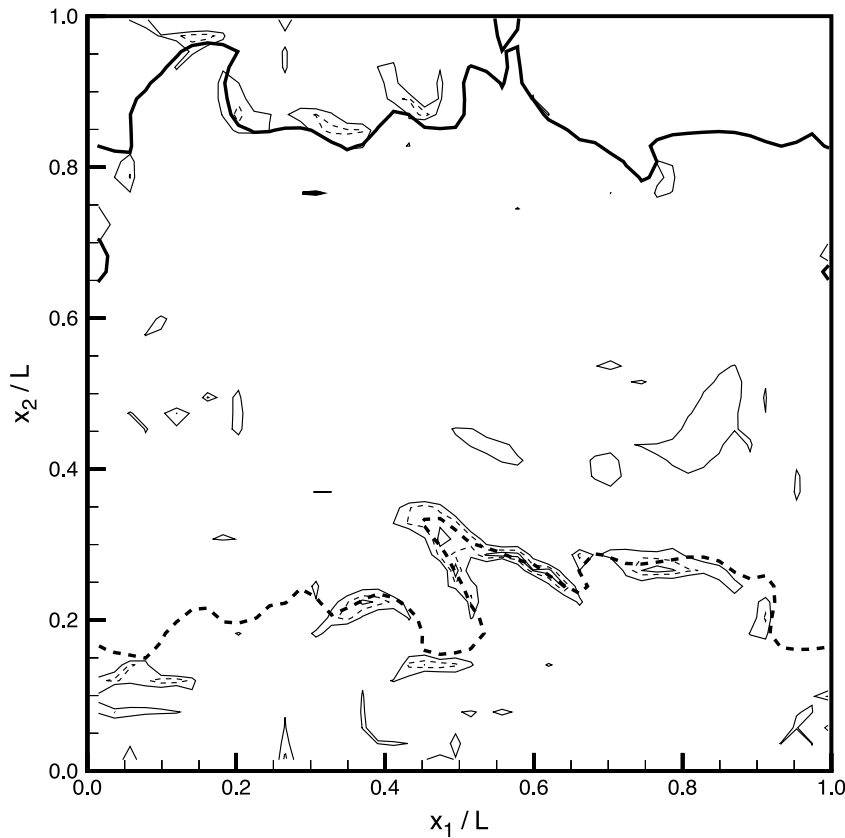


**Figure 9.** Contours of  $\log_{10}(\chi^*/\chi_q^*)$  for run 4 at time  $t/T_c = 0.39$  at slice  $x_3/L = 0.286$ . The contour levels shown are  $-0.3$  (full),  $-0.6$  (broken) and  $-1$  (full). (Only the largest levels are shown for clarity.) The bold curves are the mixture-fraction isosurface cuts: —,  $\xi = \xi_s$ ; - - -,  $\xi = -\xi_s$ .

**M** An MPEG movie associated with this figure is available from the article's abstract page in the online journal; see <http://www.iop.org>.

Average moments for the PDF of  $\ln(\chi^*)$ ,  $f_{\ln(\chi^*)}$ , are given in table 3, which shows that the scalar dissipation is very nearly log-normal. (A normal distribution has zero skewness, a kurtosis of 3 and a superskewness of 15. The PDFs and scalar dissipation moments for run 3 are not shown because the mixture fraction and hydrodynamic fields for run 3 are identical to the first two-thirds of run 2.) In each run the range of  $\chi^*$  is five decades. Only the turbulent dissipation displays similar behaviour.

The dependence of the PDF of  $\ln(\chi^*)$  on the Reynolds number is an important question, given the large variance seen at the relatively small Taylor Reynolds number of 30 here. The passive scalar study of Overholt and Pope [16] does not give moments for the PDF of  $\ln(\chi^*)$ ; therefore, a calculation very similar to run 128.4 in that report was made with a Taylor Reynolds number of 80.6, resulting in a value of the variance of  $\ln(\chi^*) = 2.9 \pm 0.2$ . As expected, there is an increase in variance with Reynolds number. Further study is needed to determine more precisely how this PDF changes with Reynolds number.

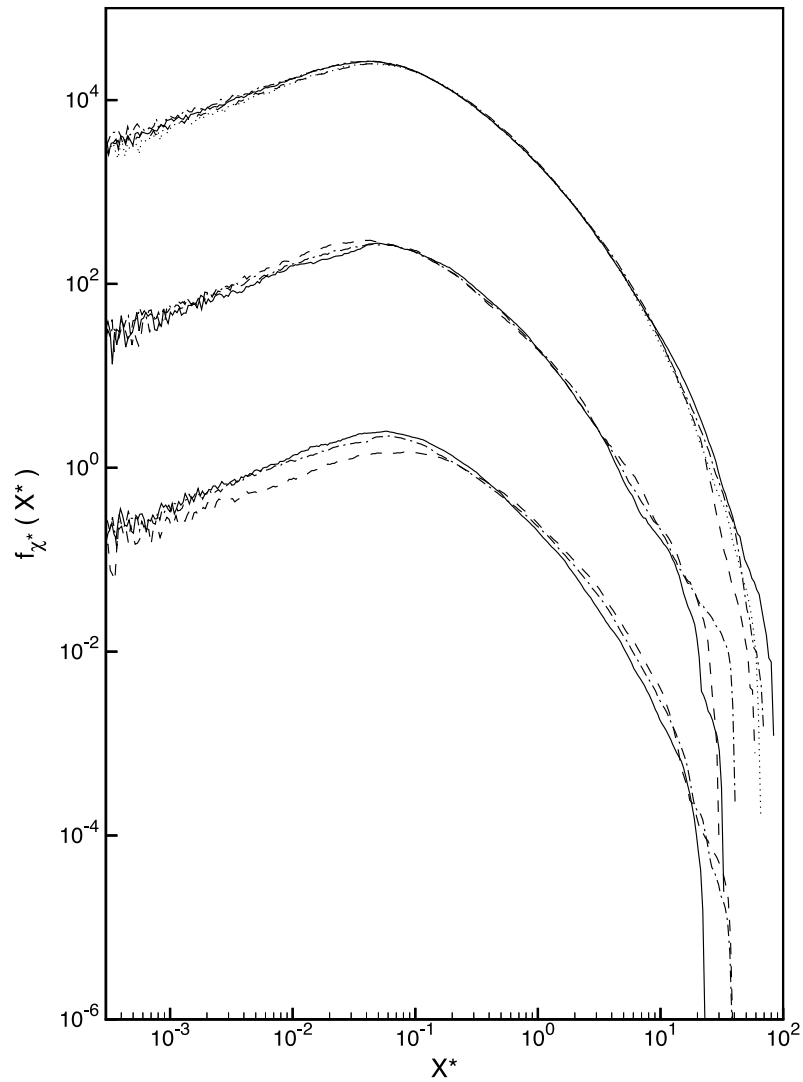


**Figure 10.** PDF  $f_{\chi^*}(X^*; t)$ . Run 1: —,  $t/T_e = 0.26$ ; — · —,  $t/T_e = 0.75$ ; - - -,  $t/T_e = 1.41$ . Run 2 (shifted up two decades): —,  $t/T_e = 0.29$ ; — · —,  $t/T_e = 0.85$ ; - - -,  $t/T_e = 1.44$ . Run 4 (shifted up four decades): —,  $t/T_e = 0.39$ ; — · —,  $t/T_e = 1.08$ ; - - -,  $t/T_e = 2.07$ ; ·····,  $t/T_e = 3.05$ .

In the interest of studying local extinction we examine the evolution of  $\chi^*$  conditioned on being in either the flame zone ( $\xi_{RF}$ ) or in the reversed zone ( $\xi_{RR}$ , see equations (15) and (16)), shown in figures 11–13. Note that these are average values. Since  $\Delta\xi_r$  is equal to 0.464, on average nearly one-half of the computational domain is within one of these two zones.

In figure 11 it can be seen that conditional  $\chi^*$  levels are much higher in the flame zone than in the reversed zone until the end of the run, leading one to anticipate a higher probability of local extinction occurring in the flame zone than in the reversed zone. The drop in  $\langle\chi^*|\xi \in \xi_{RF}\rangle$  at the end of the run is matched by an increase in  $\langle\chi^*|\xi \in \xi_{RR}\rangle$ . Runs 2 and 3 begin with moderately low and equal values of conditional  $\chi^*$  in the flame and reversed zones, followed

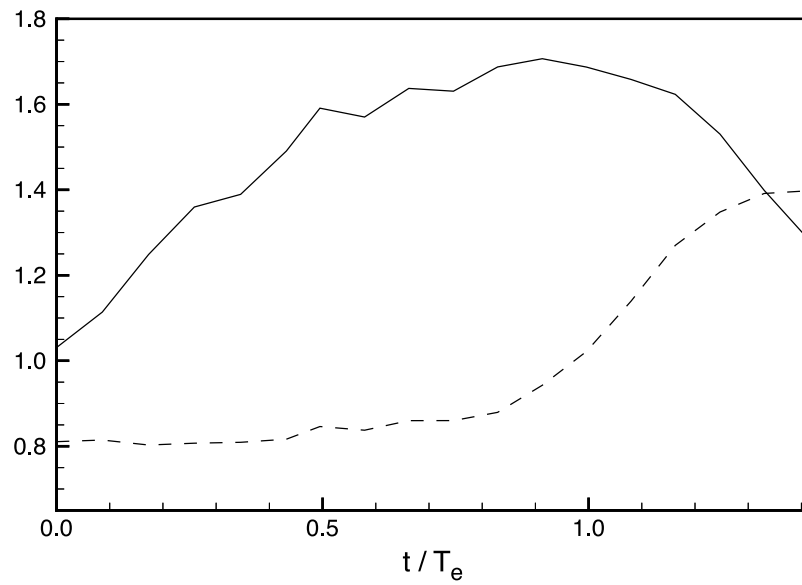


**Figure 11.** Evolution of scalar dissipation for run 1. —,  $\langle \chi^* | \xi \in \xi_{RF} \rangle$ ; - - -,  $\langle \chi^* | \xi \in \xi_{RR} \rangle$ .

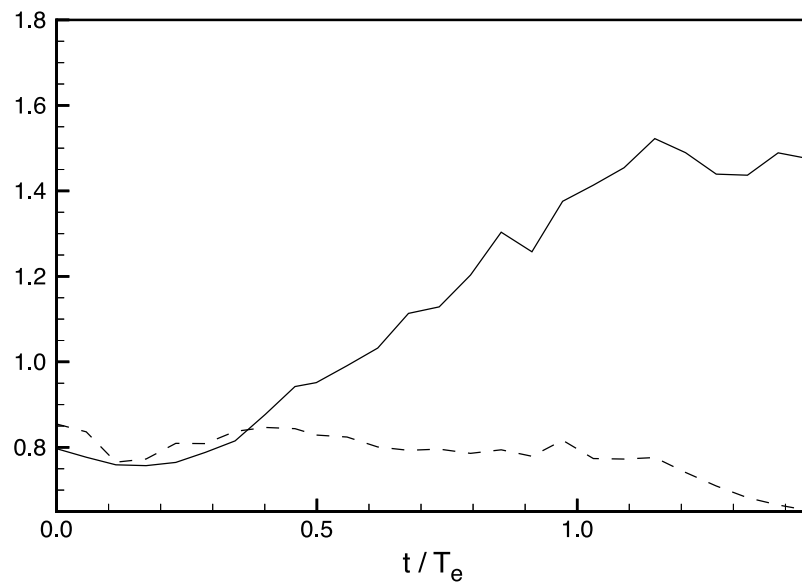


**Figure 12.** Evolution of scalar dissipation for run 2. —,  $\langle \chi^* | \xi \in \xi_{RF} \rangle$ ; - - -,  $\langle \chi^* | \xi \in \xi_{RR} \rangle$ . (Run 3 is for  $t/T_e = [0.0, 1.02]$ .)

by a significant rise in the flame-zone-conditioned value. The reversed-zone-conditioned value remains moderately low throughout. Again, it would be expected that local extinction would occur (first) in the flame zone.

Run 4 (figure 13) shows similar large-scale trends in the conditional  $\chi^*$  values; however, short-duration spikes appear in both of the curves. Accompanying the reduced  $\xi'$  in the DNS for run 4 is the reduced integral-scale size  $\ell$ . The result of this is that the largest eddies

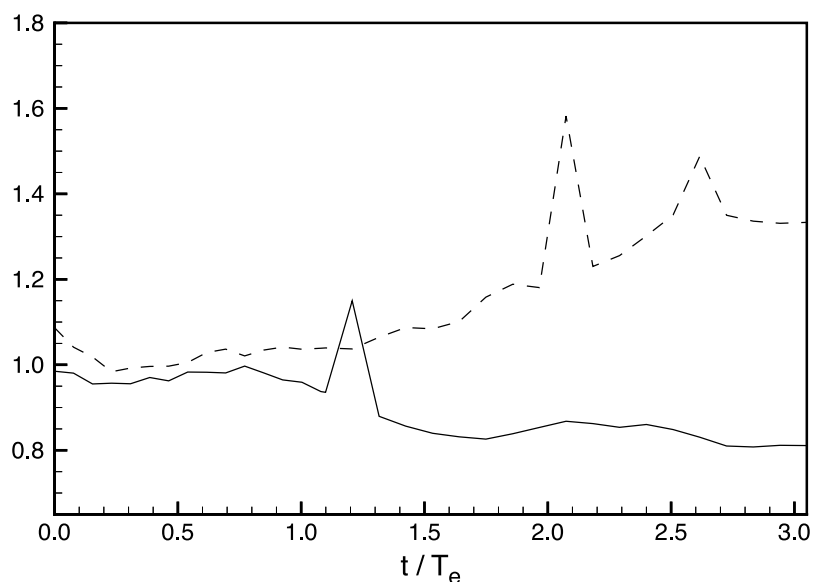


Figure 13. Evolution of scalar dissipation for run 4. —,  $\langle \chi^* | \xi \in \xi_{RF} \rangle$ ; - - -,  $\langle \chi^* | \xi \in \xi_{RR} \rangle$ .

accomplishing turbulent mixing of the flow are smaller. Hence the spikes seen in conditional  $\chi^*$  could be created by small unmixed pockets of high-scalar-dissipation fluid moving through the reaction zone. More detailed investigation is required to ascertain whether this is actually the case. (Note that the time increment for the output of the data shown in figures 11–13 is fairly large and hence each spike is composed of a single high value. For this run there are 100–150 time steps per output time step.)

Central to the preceding discussions of local extinction is the influence of local scalar dissipation. An instructive way to examine the local scalar dissipation is through its cumulative distribution function, or CDF. A good approximation for these CDFs can be formed by assuming that the PDF of  $\ln(\chi)$  is Gaussian. Figure 14 presents average CDFs of scalar dissipation divided by the critical value  $\chi_q^*$  for each run, compared with the prediction obtained by assuming that  $\chi$  is log-normal and using the average values of the mean and variance of  $\ln(\chi^*)$  obtained from the DNS. Clearly, the three runs are indistinguishable from each other, with the predicted results giving an excellent fit to the data.

It is also clear that the probability of local scalar dissipation being greater than the critical value (one minus the value of the CDF at  $\chi^*/\chi_q^* = 1$ ) is very low. This is true even of the time-dependent, conditional CDF  $\langle \chi^*/\chi_q^* | \xi \in \xi_R \rangle$  (not shown). Since local extinction does occur, as will be seen, one would expect the probability of values of  $\chi^* > \chi_q^*$  to be greater. The rarity of events with  $\chi^* > \chi_q^*$ , however, may be partly because the critical Damkohler number (and likewise  $\chi_q^*$ ) predicted by CMC is not accurate. Lee and Pope [7] found that CMC underpredicted the critical  $Da$  by a factor of two to three for values of  $\hat{\xi}_r$  similar to those in these simulations. With that in mind we denote as ‘critical probability’ the probability that  $\chi^* > \frac{1}{2}\chi_q^*$ , which is tabulated in table 6 for each run at various times.

The tabulated critical probabilities are very small, but still show the same qualitative behaviour as seen in figures 11–13. Run 1 has larger critical probabilities in the flame zone, runs 2 and 3 show a rapid increase in the flame zone values, and the end of run 4 shows an increase in critical probability in the reversed zone.

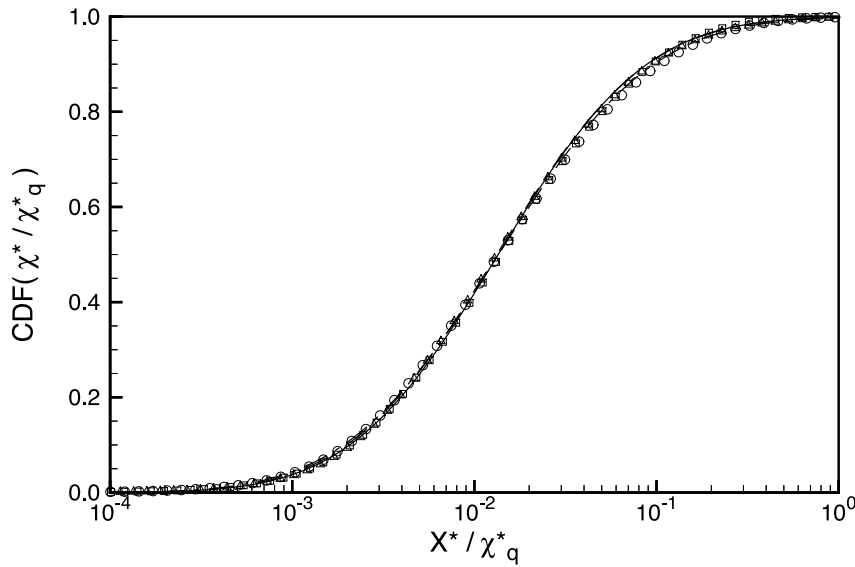


**Figure 14.** Cumulative distribution function (CDF) of scalar dissipation,  $\text{CDF}(\chi^*/\chi_q^*)$ . Log-normal prediction: —, run 1; - - -, run 2; — · —, run 4. DNS:  $\square$ , run 1;  $\triangle$ , run 2;  $\circ$ , run 4.

**Table 6.** Conditional probability that  $2\chi^* > \chi_q^*$  at various times for each run.

Run	$t/T_e$	$\text{Prob}[2\chi^* > \chi_q^*   \xi \in \xi_{RF}]$	$\text{Prob}[2\chi^* > \chi_q^*   \xi \in \xi_{RR}]$
1	0.26	0.0040	0.0009
1	0.75	0.0058	0.0004
1	1.41	0.0030	0.0017
2	0.29	0.0031	0.0053
2	0.85	0.0174	0.0080
2	1.44	0.0208	0.0005
3	0.29	0.0002	0.0000
3	0.87	0.0064	0.0011
4	0.39	0.0066	0.0075
4	1.08	0.0080	0.0071
4	2.07	0.0049	0.0076
4	3.05	0.0024	0.0117

### 4.3. Reaction progress-variable perturbation

Having examined the fluctuations in the mixture fraction, which wrinkle the flame, and the spatial variations in scalar dissipation, which can cause it to locally extinguish, we are now prepared to examine the reaction progress-variable perturbation.

Figures 15–18 give the evolution of the conditional and unconditional means of  $y^*$  (defined by equation (32)), as well as its variance. For run 1 a dramatic rise in variance from near zero is seen at the same time as, and strongly correlated with, the flame-zone-conditioned value of  $y^*$ , which is also rising, signifying local extinction beginning somewhere in the flame zone. The reversed-zone-conditioned value of  $y^*$  remains small and nearly constant throughout the simulation. In the earlier discussion of conditional  $\chi^*$  and in figure 11 it was anticipated that local extinction was more likely to occur in the flame zone since the flame-

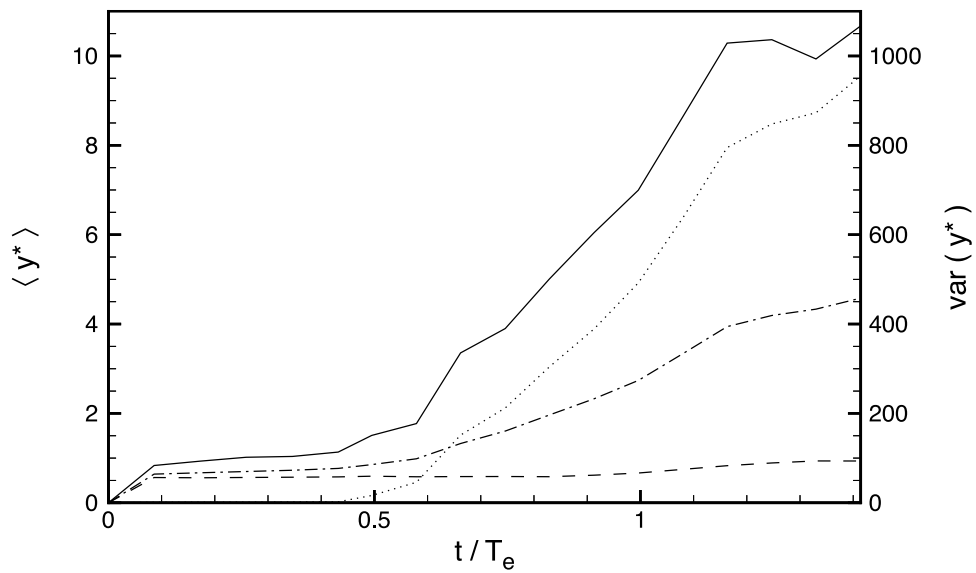


**Figure 15.** Evolution of conditional and unconditional statistics of  $y^*$  for run 1: —,  $\langle y^* | \xi \in \xi_{RF} \rangle$ ; - - -,  $\langle y^* | \xi \in \xi_{RR} \rangle$ ; — · —,  $\langle y^* \rangle$ ; ·····,  $\text{var}(y^*)$ .

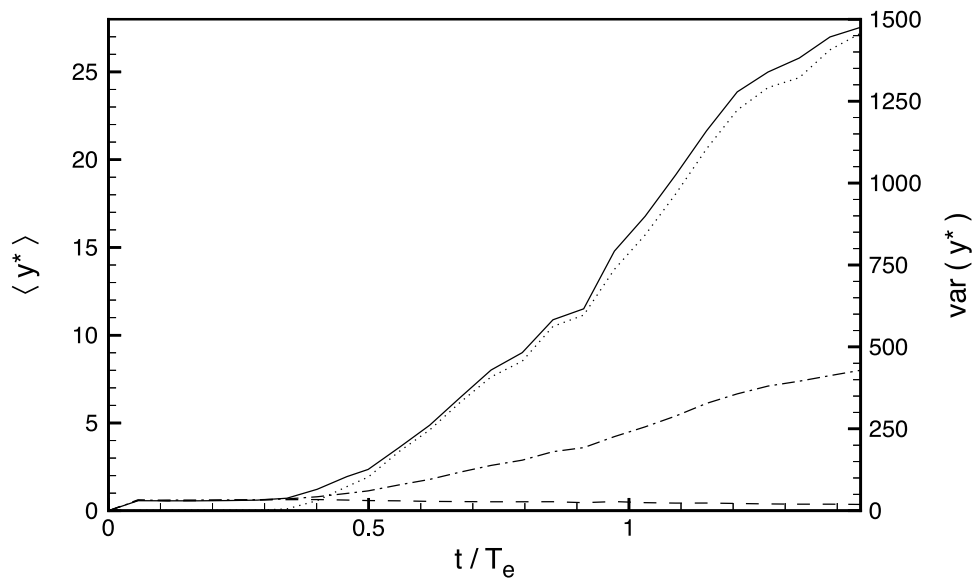


**Figure 16.** Evolution of conditional and unconditional statistics of  $y^*$  for run 2. —,  $\langle y^* | \xi \in \xi_{RF} \rangle$ ; - - -,  $\langle y^* | \xi \in \xi_{RR} \rangle$ ; — · —,  $\langle y^* \rangle$ ; ·····,  $\text{var}(y^*)$ .

zone-conditioned values of  $\chi^*$  and critical probability are also relatively high for this run, but there appears to be a time lag on the initiation of the local extinction. Given the theory that local extinction is caused by a sufficiently large blob of high-scalar-dissipation fluid intersecting the stoichiometric surface, in run 1 this chance event apparently does not occur until about  $0.5T_e$  into the run.

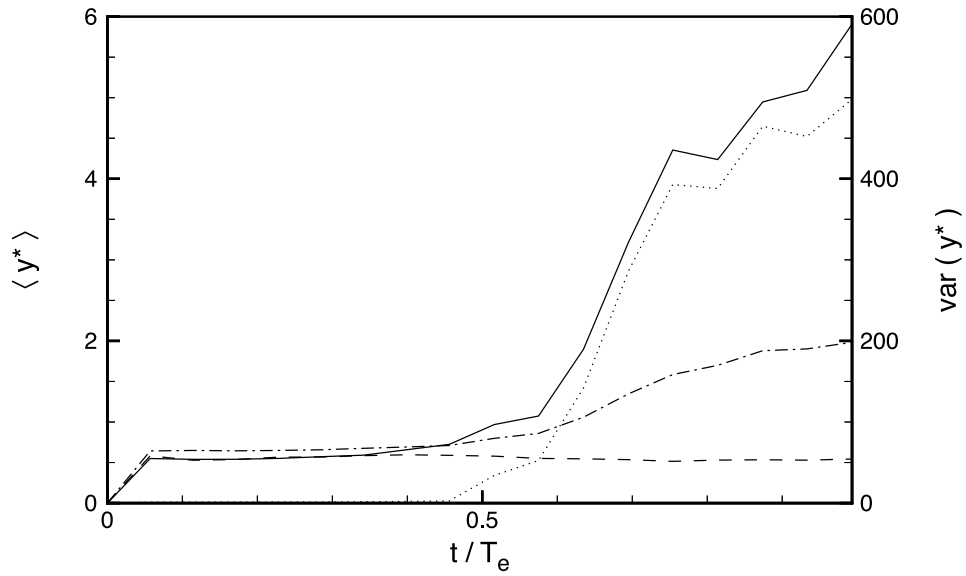


**Figure 17.** Evolution of conditional and unconditional statistics of  $y^*$  for run 3: —,  $\langle y^* | \xi \in \xi_{RF} \rangle$ ; - - -,  $\langle y^* | \xi \in \xi_{RR} \rangle$ ; — · —,  $\langle y^* \rangle$ ; ·····,  $\text{var}(y^*)$ .

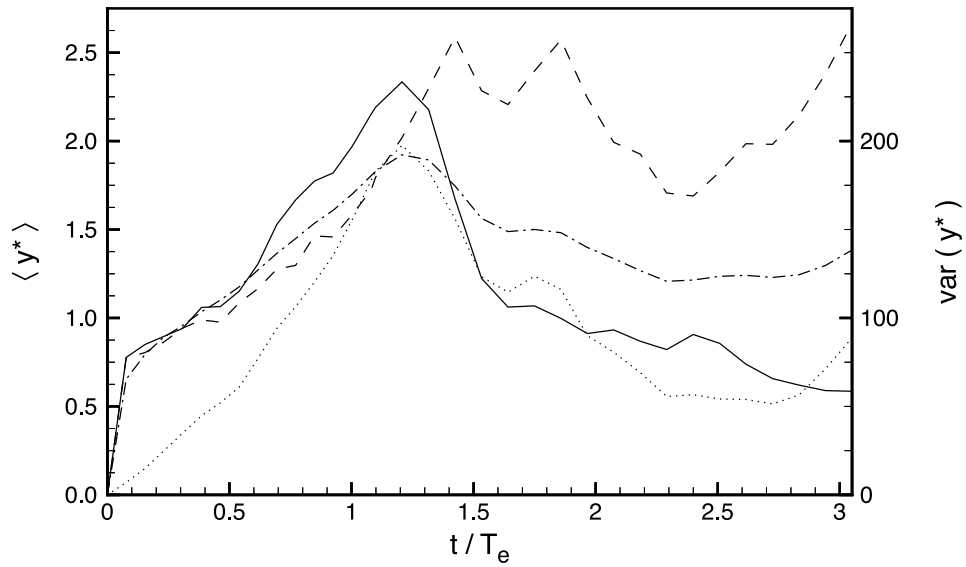


**Figure 18.** Evolution of conditional and unconditional statistics of  $y^*$  for run 4: —,  $\langle y^* | \xi \in \xi_{RF} \rangle$ ; - - -,  $\langle y^* | \xi \in \xi_{RR} \rangle$ ; — · —,  $\langle y^* \rangle$ ; ·····,  $\text{var}(y^*)$ .

Figure 16, which pertains to run 2, is qualitatively the same as figure 15, only with an even stronger local extinction. In this case the start of the local extinction correlates well with the conditional  $\chi^*$  evolution shown in figure 12 and with the large increase in the flame-zone-conditioned critical probability given in table 6. Note that the flame-zone-conditioned critical probability at time  $t/T_e = 0.29$  is relatively small, which helps explain the delay in initiation of local extinction.

Run 3 is represented by figure 17. Here, in spite of the high  $Da$  ratio, strong scalar dissipation activity forces  $\langle y^* \rangle$  to larger values, although only to about  $\frac{1}{4}$  as large a value as in run 2.

Run 4 behaves differently, with no initial quiescent period of uniform equilibrium-like behaviour as seen in the other three runs; local extinction in both the flame and the reversed zones begins immediately. After one eddy-turnover time the flame zone begins to fully reignite (i.e. local extinction begins to disappear), while the reversed zone oscillates in the appearance of continued local extinction activity. The evolution of conditional  $\chi^*$  supports this result, since it shows moderately increasing values of reversed-zone-conditioned  $\chi^*$  for the second half of the simulation, accompanied by decreasing values of flame-zone-conditioned  $\chi^*$ . The same trend is seen in the critical probabilities. This is the first simulation which continued long enough for reignition to occur, and it is especially interesting for that reason.

Conditioning on  $y$  being in one reaction zone or another is useful for observing the overall behaviour and evolution of  $y$ . However, to investigate this in more detail it is necessary to condition on the mixture fraction, i.e. to plot  $\langle y^* | \xi = \Psi \rangle$  as is shown in figures 19–22. Here, the DNS simulation results at various times are indicated with symbols (with periodicity accounted for using equations (11)–(14)), while the full curve is the CMC solution. The CMC solutions shown in each figure are obtained at the time-averaged values of  $Da$  and  $\hat{\xi}_r$  for each simulation, as given in table 1. If instead CMC solutions were calculated for each of the instantaneous values of  $Da$  and  $\hat{\xi}_r$  corresponding to the DNS output times, only very small ( $\ll y_{\text{ref}}$ ) variations would be seen.

Figure 19 for run 1 dramatically illustrates the local extinction occurring in the flame zone, while the reversed zone maintains a profile remarkably close to the CMC solution. Several characteristics should be noted, the first being the manner in which the local extinction occurs. Since extinction occurs when microscale mixing overpowers the reaction rate and microscale mixing is dominated by  $Y_c''$ , which is by far the largest on the stoichiometric surface, it is expected that local extinction begins on the stoichiometric surface and then spreads to other values of  $\xi$ . Therefore, we expect that  $\langle y^* | \xi = \Psi \rangle$  will show the initiation of local extinction as centred on the stoichiometric mixture fraction, with the largest values there (i.e. at  $\xi = \xi_s$ ). This is clearly seen in figure 19 where  $\langle y^* | \xi = \xi_s \rangle$  does increase first, pulling the rest of the profile away from equilibrium.

In the reversed zone notice a slight lifting of  $y^*$  at the very last time shown, as anticipated from the evolution of the reversed-zone-conditioned  $\chi^*$  in figure 11. The first two times show almost identical  $y^*$  profiles, slightly below the CMC solution. However, at the final time  $\langle y^* | \xi = -\xi_s \rangle$  has risen to just above the CMC solution.

The second characteristic to note is the asymmetry of the flame zone profile at the earliest time (i.e. for  $\xi > 0.5$ ). The precise reason for this asymmetry is unknown, but several possible causes will be suggested. This is a conditional value, therefore statistics could be the reason (e.g. high statistical variability in that region, perhaps due to very few samples). Another possibility is that microscale mixing for that region was initially small, slowing down the departure from the initial condition. No other similar occurrence of such an asymmetry was observed in the results.

Since runs 2 and 3 share the same hydrodynamic and mixture-fraction fields, figures 20 and 21 show the effect of differing  $Da$ . For one, the profile of the solution changes slightly as  $Da$  increases (i.e. lower stoichiometric value relative to the ‘shoulders’ on either side). The primary feature to note, however, is the decreased extent of local extinction in run 3 as compared to run 2 at the same time. This can be seen in the maximum value of the second output time step ( $t/T_e = 0.85$  for run 2 and 0.87 for run 3), which is twice as large in run 2 (about 13) as in run 3 (about 7). This is the anticipated result, of course.



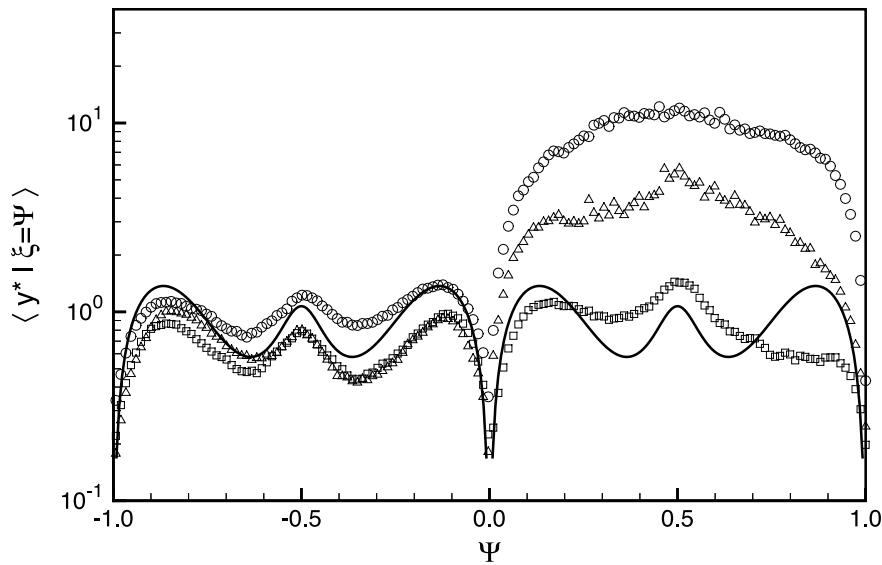


Figure 19. Conditional  $\langle y^* | \xi = \Psi \rangle$  for run 1.  $\square$ ,  $t/T_e = 0.26$ ;  $\triangle$ ,  $t/T_e = 0.75$ ;  $\circ$ ,  $t/T_e = 1.41$ ; —, CMC.

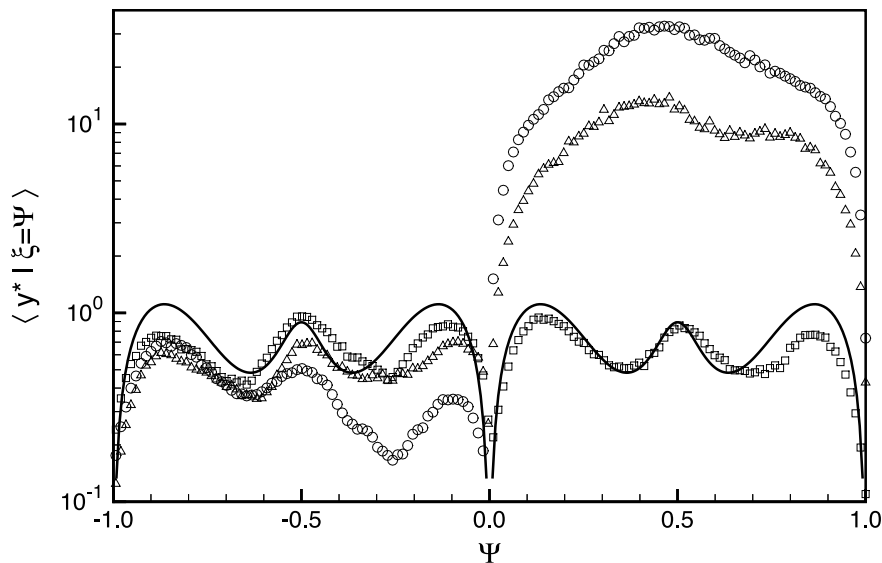


Figure 20. Conditional  $\langle y^* | \xi = \Psi \rangle$  for run 2.  $\square$ ,  $t/T_e = 0.29$ ;  $\triangle$ ,  $t/T_e = 0.85$ ;  $\circ$ ,  $t/T_e = 1.44$ ; —, CMC.

Much more staid behaviour is observed in run 4 (figure 22) where the reaction zone is almost twice as wide as the rms fluctuation of  $\xi$ . As also seen in the temporal evolution of  $y^*$  (figure 18), early on there is a small local extinction in the flame zone which then reignites, resulting in the last two profiles lying very close to the CMC solution. In the reversed zone a small local extinction is occurring throughout most of the simulation, and is centred on the stoichiometric value.

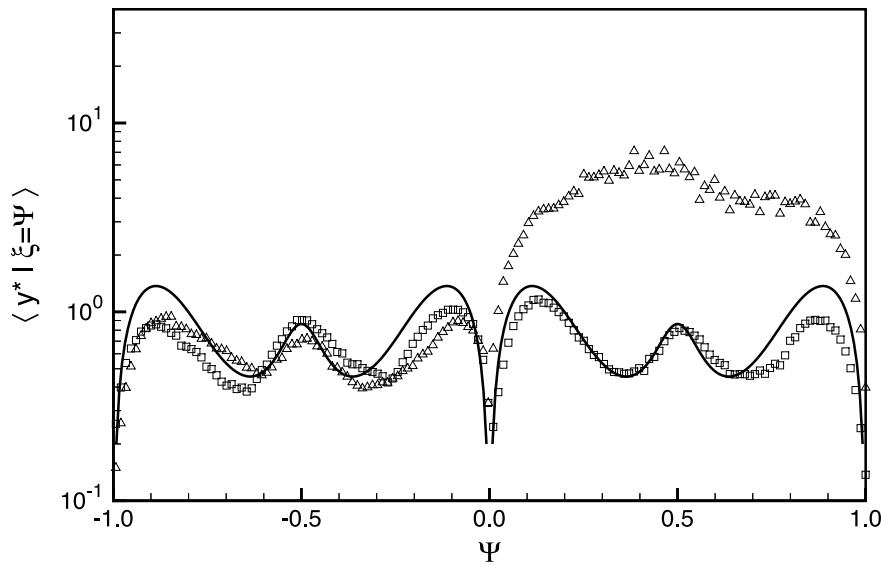


Figure 21. Conditional  $\langle y^* | \xi = \Psi \rangle$  for run 3.  $\square$ ,  $t/T_e = 0.29$ ;  $\triangle$ ,  $t/T_e = 0.87$ ; —, CMC.

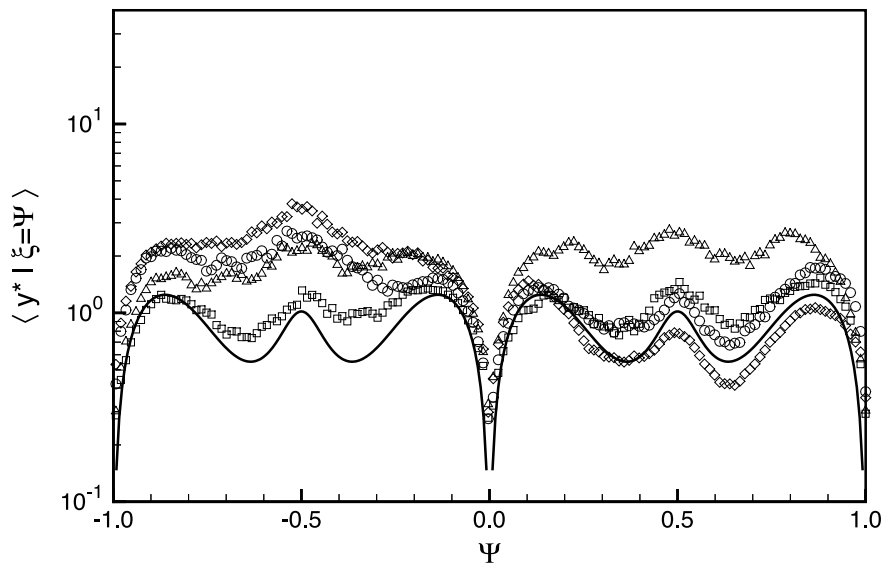


Figure 22. Conditional  $\langle y^* | \xi = \Psi \rangle$  for run 4.  $\square$ ,  $t/T_e = 0.39$ ;  $\triangle$ ,  $t/T_e = 1.08$ ;  $\circ$ ,  $t/T_e = 2.07$ ;  $\diamond$ ,  $t/T_e = 3.05$ ; —, CMC.

After seeing so clearly the effect of local scalar dissipation on the results, it should be emphasized that most turbulent combustion models are based on the volume-averaged mean scalar dissipation,  $\langle \chi \rangle$ , and thereby do not account for the local variations. This includes the CMC and QEDR models. An exception to the rule is the Lagrangian spectral relaxation model of Fox [42]. The effect of local scalar dissipation is illustrated here by using the CMC and QEDR models *with the local  $\chi$  substituted for  $\langle \chi \rangle$* , resulting in a close comparison with the


DNS results. See the report by Overholt and Pope [9] for more details on the model solutions presented here.

Returning again to run 1, figure 23 compares the flame-zone- and reversed-zone-conditioned values of  $y^*$ , conditioned also on the local scalar dissipation, to CMC and QEDR solutions. The rightmost end of the CMC line terminates in an 'X' symbol, corresponding to the predicted extinction value. The QEDR line extends to the largest value of  $\chi^*$  for which there exists a solution to  $y^*$  for all values of  $\xi$  in the reaction zone. Overall a strong dependence of conditional  $y^*$  on local  $\chi^*$  is seen for all  $\chi$  values significantly greater than  $2\Gamma\beta^2$ . CMC and QEDR give almost identical results, both slightly overpredicting the DNS when  $\chi^* \geq 10^{-1}$  and when there is no local extinction. As noted earlier, the reversed zone remains fully reacting throughout the run. However, local extinction does occur in the flame zone, beginning at the largest value of scalar dissipation and then propagating to smaller values.

A normalized, critical value of scalar dissipation was defined earlier by equation (33). The value of  $\chi_q^*$  is not indicated in these figures; however, the CMC predicted extinction values (denoted by 'X' symbols) closely correspond to the  $\chi_q^*$  values. In all of the runs a general behaviour is seen: if values of  $\chi^*$  significantly greater than  $\chi_q^*$  exist then local extinction usually also exists. Exceptions to this rule can be explained by realizing that a single occurrence of a large value of  $\chi^*$  may not be sufficient to cause local extinction. A sufficiently large blob of high-scalar-dissipation fluid may have to intersect the stoichiometric isosurface to bring about local extinction. In run 1 (figure 23) at the earliest time the symbols ( $\square$ ) all have values of  $\chi^*$  less than  $\chi_q^*$ , which explains why it is still fully reacting at that time (see figures 19 and 15). The following two output times show values of  $\chi^*$  greater than  $\chi_q^*$  as well as local extinction.

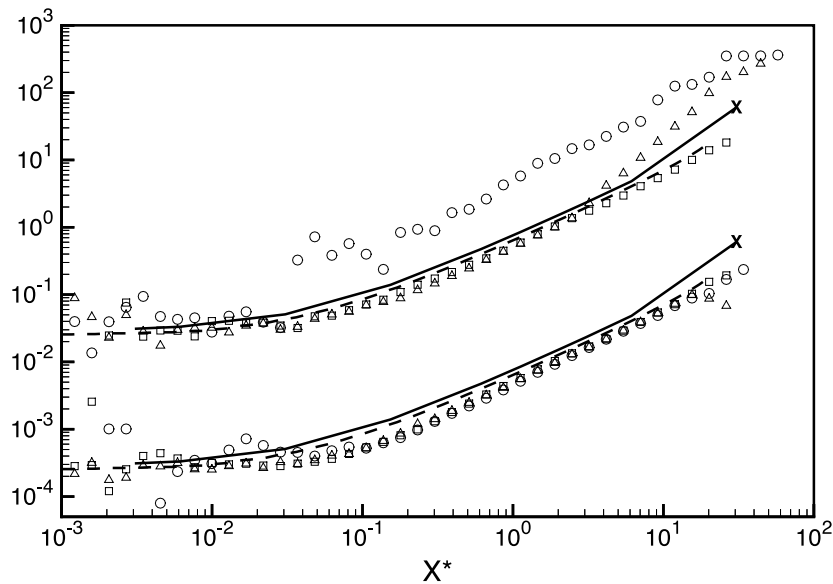


**Figure 23.** Conditional  $\langle y^* | \xi \in \xi_{RF}, \chi^* = X^* \rangle$ , and shifted down two decades  $\langle y^* | \xi \in \xi_{RR}, \chi^* = X^* \rangle$ , for run 1.  $\square$ ,  $t/T_e = 0.26$ ;  $\triangle$ ,  $t/T_e = 0.75$ ;  $\circ$ ,  $t/T_e = 1.41$ ; —, CMC; - - -, QEDR. The CMC critical extinction value is denoted by an 'X' symbol.

 An MPEG movie associated with this figure is available from the article's abstract page in the online journal; see <http://www.iop.org>.

Note that once local extinction is triggered the disturbance propagates to values of  $\chi^*$  much less than  $\chi_q^*$ .

Figures 24 and 25 show the same close comparison between the DNS data and the models, with the same pattern of local extinction initiating at values of  $\chi^* > \chi_q^*$ . Also, the lesser extent of local extinction in the higher  $Da$  ratio run can be seen in the decreased propagation (of  $\Delta$  symbols) toward smaller values of  $\chi^*$ . In the reversed zone of run 2 values of  $\chi^*$  do exceed  $\chi_q^*$  without resulting in local extinction. However, based on figure 12 it appears that the majority of the reversed reactive region is experiencing below-average levels of  $\chi^*$ , which could explain why local extinction has not occurred.


The results for run 4 shown in figure 26 are similar. As noted in the discussion of figure 22, the local extinction experienced in this simulation is less extensive, which is manifest here in both the smaller deviations of conditional  $y^*$  from its fully reacting value and also in the smaller distance in which the extinction disturbance propagates to the left (i.e. towards smaller values of  $\chi^*$ ).

In summary, doubly conditioning  $y^*$  on the local scalar dissipation and on being in the reaction zone clearly shows a strong dependence on the local scalar dissipation to the point that the occurrence of local extinction can almost be predicted based on whether or not points exist or have existed with  $\chi^*$  significantly greater than  $\chi_q^*$ .

In order to better understand figures 23–26, it is useful to examine the doubly conditioned quantity  $\langle y^* | \xi = \Psi, \chi^* = X^* \rangle$ . Only a few sample results are shown due to lack of space; however, they qualitatively represent the behaviour seen throughout. Figures 27 and 28 show the evolution of  $y^*$  thus conditioned in run 3. At first a uniform behaviour is seen. Then, as local extinction begins, values of  $y^*$  at large  $\chi^*$  rapidly increase and the disturbance spreads

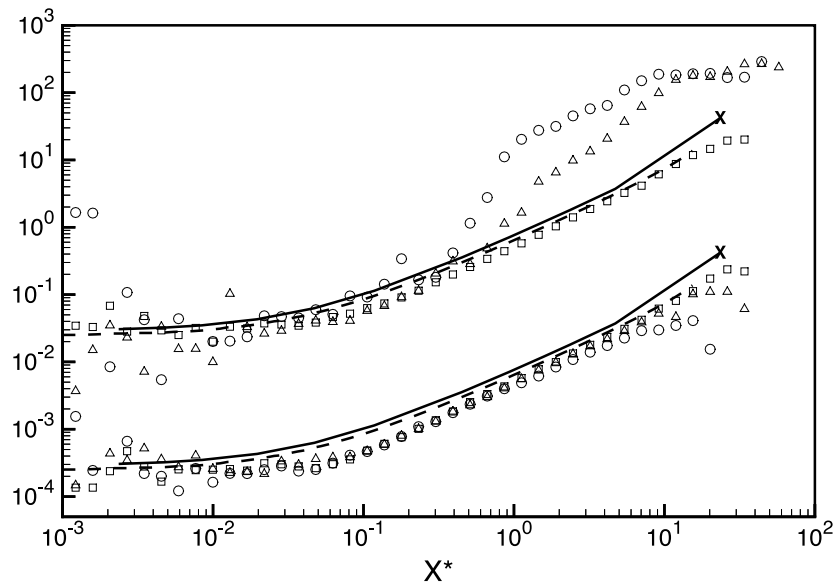


**Figure 24.** Conditional  $\langle y^* | \xi \in \xi_{RF}, \chi^* = X^* \rangle$ , and shifted down two decades  $\langle y^* | \xi \in \xi_{RR}, \chi^* = X^* \rangle$ , for run 2.  $\square$ ,  $t/T_e = 0.29$ ;  $\triangle$ ,  $t/T_e = 0.85$ ;  $\circ$ ,  $t/T_e = 1.44$ ; —, CMC; - - -, QEDR. The CMC critical extinction value is denoted by an 'X' symbol.

 An MPEG movie associated with this figure is available from the article's abstract page in the online journal; see <http://www.iop.org>.

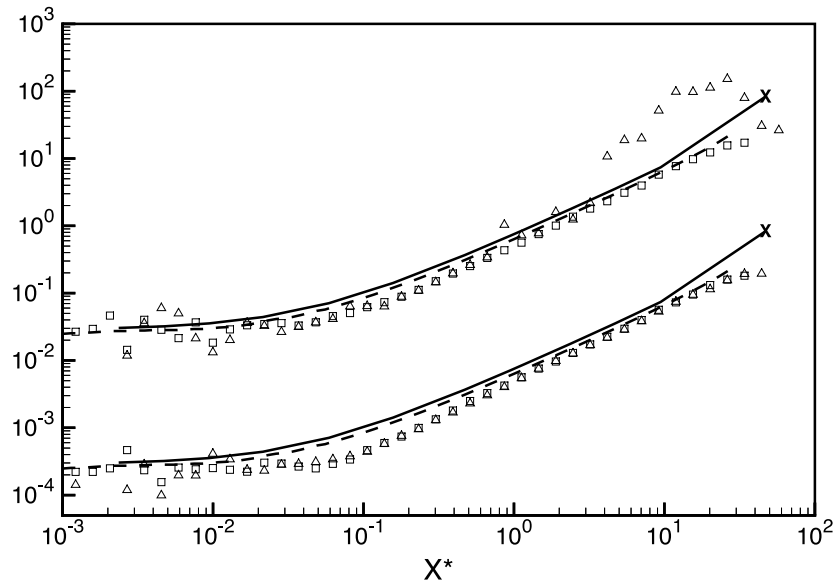


**Figure 25.** Conditional  $\langle y^* | \xi \in \xi_{RF}, \chi^* = X^* \rangle$ , and shifted down two decades  $\langle y^* | \xi \in \xi_{RR}, \chi^* = X^* \rangle$ , for run 3.  $\square$ ,  $t/T_e = 0.29$ ;  $\triangle$ ,  $t/T_e = 0.87$ ; —, CMC; - - -, QEDR. The CMC critical extinction value is denoted by an 'X' symbol.

**[M]** An MPEG movie associated with this figure is available from the article's abstract page in the online journal; see <http://www.iop.org>.

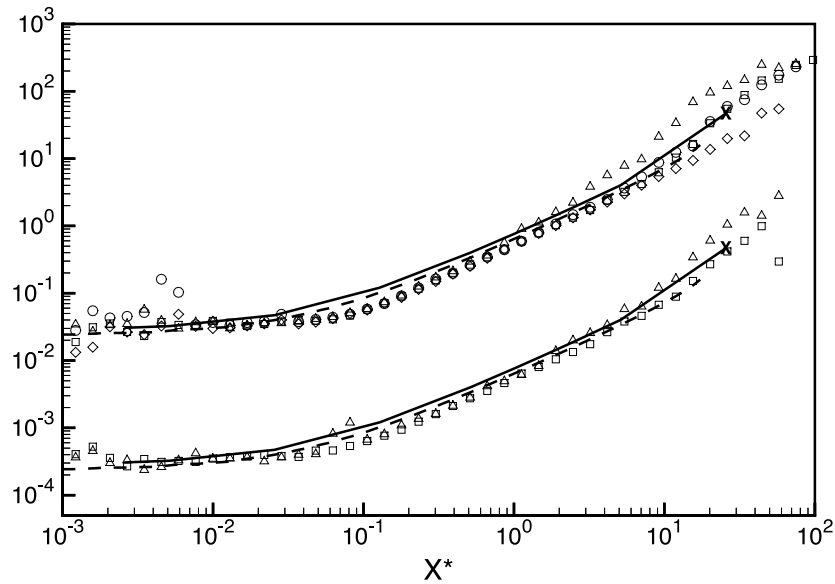


**Figure 26.** Conditional  $\langle y^* | \xi \in \xi_{RF}, \chi^* = X^* \rangle$ , and shifted down two decades  $\langle y^* | \xi \in \xi_{RR}, \chi^* = X^* \rangle$ , for run 4.  $\square$ ,  $t/T_e = 0.39$ ;  $\triangle$ ,  $t/T_e = 1.08$ ;  $\circ$ ,  $t/T_e = 2.07$ ;  $\diamond$ ,  $t/T_e = 3.05$ ; —, CMC; - - -, QEDR. The CMC critical extinction value is denoted by an 'X' symbol.

**[M]** An MPEG movie associated with this figure is available from the article's abstract page in the online journal; see <http://www.iop.org>.

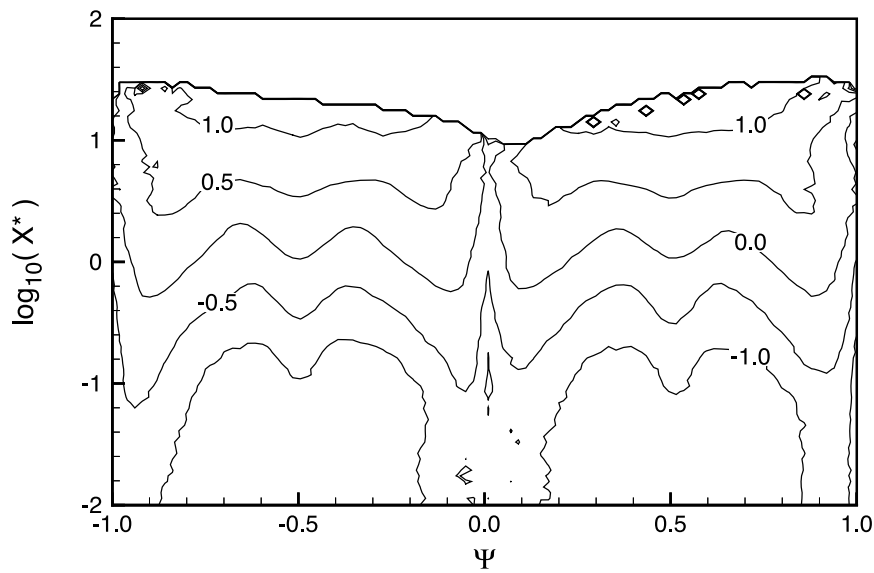


**Figure 27.** Conditional  $\langle y^* | \xi = \Psi, \chi^* = X^* \rangle$  for run 3 at time  $t/T_e = 0.29$ . Contour level values are for  $\log_{10}(y^*)$ .

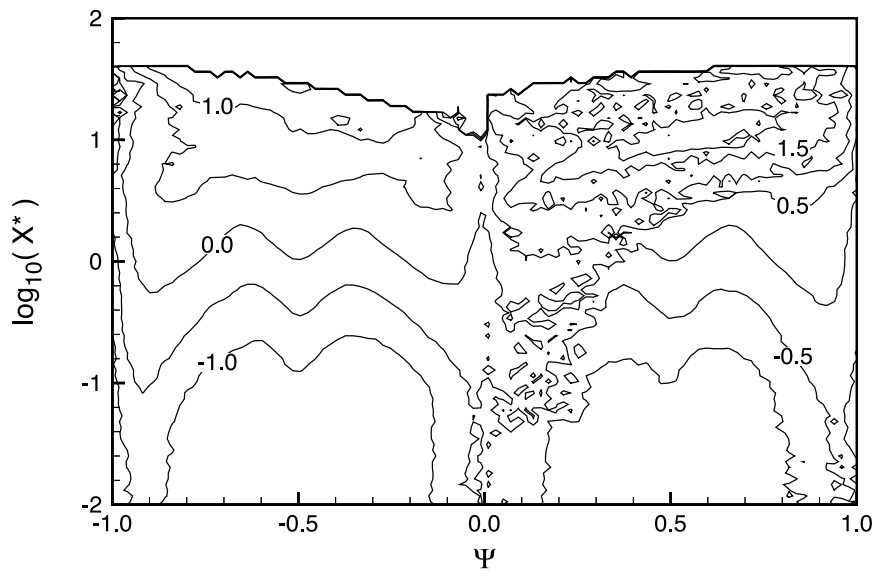


**Figure 28.** Conditional  $\langle y^* | \xi = \Psi, \chi^* = X^* \rangle$  for run 3 at time  $t/T_e = 0.87$ . Contour level values are for  $\log_{10}(y^*)$ .

to neighbouring regions of the  $\xi$ - $\chi$  space. These figures should be compared with the QEDR and CMC solutions for run 3, shown in figure 29. Again, the solutions are calculated to the largest values of  $\chi^*$  possible. Clearly the CMC solution corresponds very closely to figure 27. It can also be seen that the QEDR solution is best inside the reaction zone and deteriorates outside. Other figures (not shown) show that, after local extinction passes and reignition occurs,  $\langle y^* | \xi = \Psi, \chi^* = X^* \rangle$  returns to its undisturbed shape.

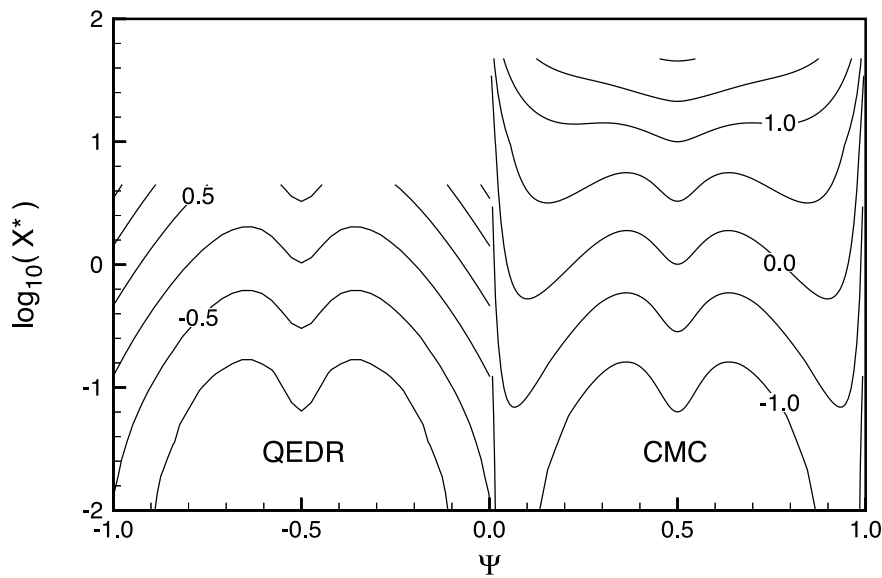


**Figure 29.** Conditional  $\langle y^* | \xi = \Psi, \chi^* = X^* \rangle$  for run 3 as predicted by QEDR ( $\xi < 0$ ) and CMC ( $\xi > 0$ ). Contour level values are for  $\log_{10}(y^*)$ .

Figure 30 shows a typical local extinction, here occurring in the reversed zone of run 4. Only one slice is shown; however, that slice is taken through the middle of the local extinction, which has a third dimension roughly equal to the extent of the disturbance along  $x_1$ . This is the same slice as was shown in figure 9, where it was noted that the maximum levels of  $\chi^*$  occurred on the stoichiometric surface in the reversed zone. That is the same location where the local extinction is occurring in this figure, validating the theory that local extinction is brought on by large values of local scalar dissipation. (Note for the electronic version: an MPEG movie comparing the evolution of the  $y^*$  and  $\chi^*$  fields is available.)

In summary, these results all agree with the following local extinction mechanism. It is known that local extinction is driven by microscale mixing overpowering the reaction rate. Microscale mixing is by far the largest near the stoichiometric surface due to  $Y_e''$ , hence local extinction begins there. Local extinction begins, then, when a pocket or small region of high local-scalar dissipation intersects the stoichiometric surface. In order for the disturbance to exist for any significant period of time that pocket must be large enough in magnitude and extent to drive the local  $y$  past the maximum reaction rate (for the thermochemistry parameters chosen here, at  $\xi = \xi_s$  the maximum reaction rate occurs for  $y = 0.094$ ), after which the reaction rate decreases with increasing  $y$ , allowing  $y$  to accelerate towards  $Y_e$  ( $Y = 0$ ).

This examination would not be complete without a look at the PDF of  $y^*$  ( $y^*$  is defined in equation (32)), given in figure 31. It is evident that the large majority of the flow in all the runs is undergoing stable reaction or fully lit, with  $y$  near zero. As the first three runs progress, however, the local extinction that occurs manifests itself in the rising of the tail of the PDF and subsequent extension to larger values of the  $y^*$  sample-space variable  $Y^*$ . This phenomenon is also present in run 4, although less dramatic.

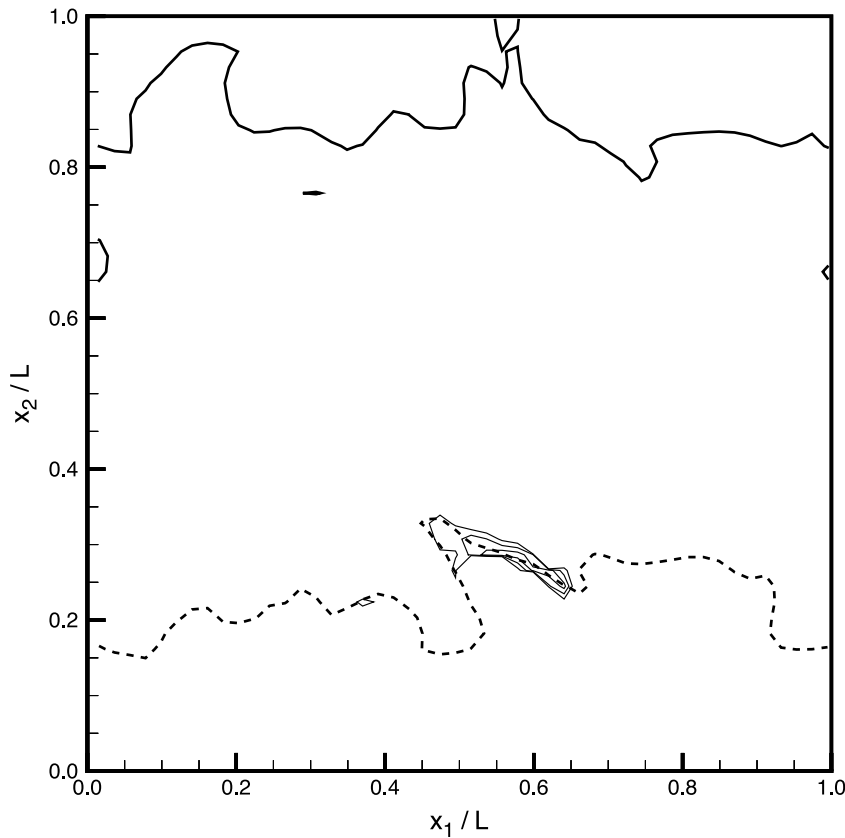


**Figure 30.** Contours of  $\log_{10}(y^*)$  for run 4 at time  $t/T_c = 0.39$  for slice  $x_3/L = 0.286$ . Contour levels are 1, 1.5 and 2. The bold curves are the mixture-fraction isosurface cuts: —,  $\xi = \xi_s$ ; - - -,  $\xi = -\xi_s$ .

**M** An MPEG movie associated with this figure is available from the article's abstract page in the online journal; see <http://www.iop.org>.

## 5. Conclusions

Clearly the PRZ model flow (periodic reaction zones) is a useful one for studying non-premixed turbulent reaction. It has been shown to be accessible to DNS, and results thereby obtained can be compared with CMC and QEDR model predictions, PDF simulations [9] and other calculations.

The parameter space for PRZ is composed of the Reynolds number, the Damkohler number and the reaction zone thickness parameter,  $\hat{\xi}_r = \Delta \xi_r / \xi'$ .

Large intermittency or spatial variability was found in the scalar dissipation, which has a profound effect on the DNS results. A mechanism for local extinction consistent with the results of this study is as follows: local extinction is initiated when a sufficiently large pocket of high-scalar-dissipation fluid intersects a stoichiometric mixture-fraction surface, increasing the strength of microscale mixing to well beyond that of the reaction rate. Local extinction occurred in this study even when the Damkohler number was 25 times the critical value, due to very large variance in the scalar dissipation ( $\text{var}[\ln(\chi/\langle\chi\rangle)] \approx 2.2$ ).



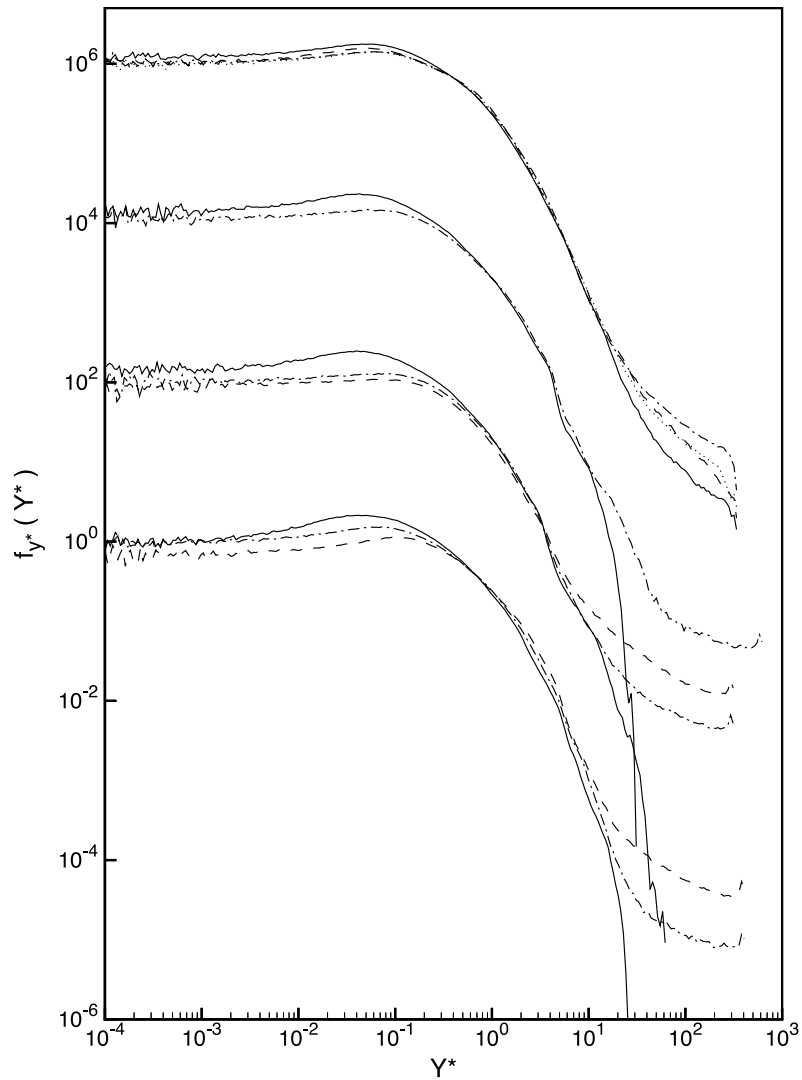


**Figure 31.** PDF  $f_{y^*}(Y^*; t)$ . Run 1: —,  $t/T_e = 0.26$ ; — · —,  $t/T_e = 0.75$ ; - - - -,  $t/T_e = 1.41$ . Run 2 (shifted up two decades): —,  $t/T_e = 0.29$ ; — · —,  $t/T_e = 0.85$ ; - - - -,  $t/T_e = 1.44$ . Run 3 (shifted up four decades): —,  $t/T_e = 0.29$ ; — · —,  $t/T_e = 0.87$ . Run 4 (shifted up six decades): —,  $t/T_e = 0.39$ ; — · —,  $t/T_e = 1.08$ ; - - - -,  $t/T_e = 2.07$ ; ·····,  $t/T_e = 3.05$ .

Both (first-moment) CMC and QEDR model predictions, based on the local  $\chi$ , gave remarkably good agreement with the DNS for regions of the flow where local extinction was not present. CMC gave the best agreement for the conditional  $\langle y^* | \xi = \Psi, \chi^* = X^* \rangle$ , and also matched the DNS very well for the conditional  $\langle y^* | \xi = \Psi \rangle$ . Higher-order conditional moment closures were not considered in this study, but a future comparison with these results would be interesting.

In summary, the value of including the scalar dissipation fluctuation in mixing models, such as Fox is doing [42], is substantiated and shown to be essential for the prediction of local extinction.

### Acknowledgments

We gratefully acknowledge support from the Department of Energy, grant no DE-FG02-90ER 14128. Supercomputing resources were provided by the Cornell Theory Center. We would also like to thank our Theory Center consultant, Dr John Zollweg, for his assistance.

### Appendix A. Thermochemistry details

The reaction rate term,  $S(\xi, Y)$ , is from the self-similar model thermochemistry developed by Subramaniam [11] for the reversible, finite-rate reaction



where  $Y_F$ ,  $Y_O$  and  $Y$  represent the mass fractions of fuel, oxidizer and product, respectively, and  $r$  is the stoichiometric proportion of the oxidizer to fuel mass fraction. At chemical equilibrium the progress variable  $Y$  takes on the equilibrium value  $Y_e$ , which is specified as an analytic function of the mixture fraction,  $\xi$ , and its stoichiometric value,  $\xi_s$ . The reaction rate, then, is defined as an analytic function of the composition  $\xi-Y$ . Salient details of the chemistry definition are given in subsections A.2 and A.3. First, however, the concept of self-similarity is addressed, which motivated much of this thermochemistry's development.

#### A.1. Self-similarity

The primary thermochemistry parameters are  $\Delta\xi_r$  and  $\tau^*$ , which in turn determine the reaction zone thickness  $\hat{\xi}_r \equiv \Delta\xi_r/\xi'$  and  $Da$ . Since  $Da$  and  $\hat{\xi}_r$  need to parametrize the PRZ model problem solution completely, for a fixed Reynolds number, they must completely describe the thermochemistry. This defines self-similarity for this thermochemistry, such that solutions for a given  $\hat{\xi}_r$ , with differing values of  $\Delta\xi_r$ , are the same. One outcome of self-similarity is the requirement that the ratio between the two mixture-fraction scales in the reaction zone,  $\Delta\xi_r$  and  $\Delta\xi_e$ , remains constant [11].

The thermochemistry of Lee and Pope [7] does not possess this property, although it is very similar to this thermochemistry in other ways. They determined the equilibrium value of the progress variable,  $Y_e$ , with the specification of an equilibrium constant  $K$  and a stoichiometric value of the mixture fraction,  $\xi_s$ . Therefore, for a given  $\xi_s$  the mixture-fraction scale  $\Delta\xi_e$  is controlled by  $K$ . However, it is not possible to vary  $\Delta\xi_r$  using  $K$  while keeping the ratio  $\Delta\xi_r/\Delta\xi_e$  and other parameters constant, as required.

Therefore, Subramaniam [11] developed a self-similar thermochemistry as a one-parameter family of  $Y_e(\xi)-\tilde{S}(\xi, y)$  functions that preserves the scaling of the terms in the scaled evolution equation for  $\langle y \rangle$  and maintains the ratio  $\Delta\xi_r/\Delta\xi_e$ . This allows the reaction zone width,  $\Delta\xi_r$ , to be varied while not affecting the scaling underlying the thermochemistry.

#### A.2. Equilibrium function, $Y_e(\xi)$ , for the symmetric case

The model thermochemistry of Subramaniam [11] is defined for any value of stoichiometric mixture fraction,  $\xi_s$ ; however, the symmetric case was chosen for this work, with  $\xi_s = \frac{1}{2}$ . The equilibrium function  $\bar{Y}_e$  is specified as a function of  $z \equiv \xi - \xi_s$  such that  $\bar{Y}_e(z) = Y_e(\xi)$ . Using the Cauchy distribution, the second derivative,  $\bar{Y}_e''$ , is defined as

$$\frac{d^2\bar{Y}_e}{dz^2} = -\frac{4}{\pi\Delta\xi_e} \frac{1}{[1+(z/\Delta\xi_e)^2]}. \quad (\text{A.2})$$

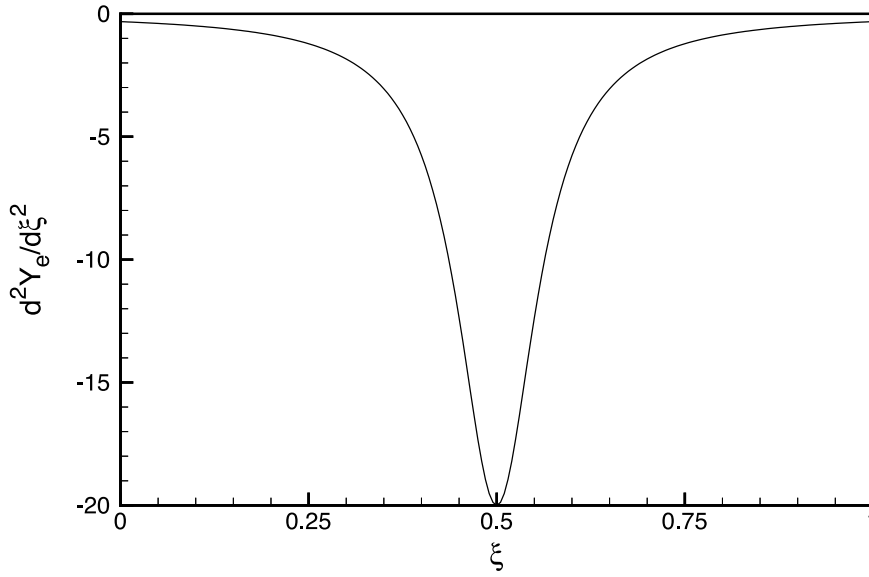


**Figure A1.** Second derivative of the equilibrium function,  $Y_e''(\xi)$ .  $C = 0.5289$ ,  $B = 0.6684$  and  $\Delta\xi_e = 0.06366$ .

Integrating twice gives

$$\bar{Y}_e(z) = -\frac{4}{\pi} z \arctan\left(\frac{z}{\Delta\xi_e}\right) + \frac{2\Delta\xi_e}{\pi} \ln\left[1 + \left(\frac{z}{\Delta\xi_e}\right)^2\right] + c \quad (\text{A.3})$$

where  $c$  is

$$c = \frac{2}{\pi} \arctan\left(\frac{1}{2\Delta\xi_e}\right) - \frac{2\Delta\xi_e}{\pi} \ln\left[1 + \left(\frac{1}{2\Delta\xi_e}\right)^2\right]. \quad (\text{A.4})$$

The shape of  $Y_e''$  is shown in figure A1 for the thermochemistry parameters chosen for this study.

### A.3. Reaction rate function

The reaction rate function is written as

$$S(\xi, Y) = \tilde{S}(\xi, y) = \bar{S}(\xi, y)/\tau_c \quad (\text{A.5})$$

where  $\tau_c$  is the chemical time scale which determines the magnitude of the reaction rate with the shape of  $\bar{S}$ , and is related to  $\tau^*$  as

$$\tau^* \equiv \frac{\tau_c}{B \exp(1)} \quad (\text{A.6})$$

with  $B$  being a specified parameter. For self-similarity the ratio  $\Delta\xi_r/\Delta\xi_e$  must be constant, requiring

$$\bar{S}(\xi, y; \Delta\xi_r/\Delta\xi_e, \Delta\xi_e) = \bar{S}(\hat{\xi}, \hat{y}; \Delta\xi_e) \quad (\text{A.7})$$

$$\bar{S}(\hat{\xi}, \hat{y}; \Delta\xi_e) = \hat{S}(\hat{\xi}, \hat{y}) \quad (\text{A.8})$$

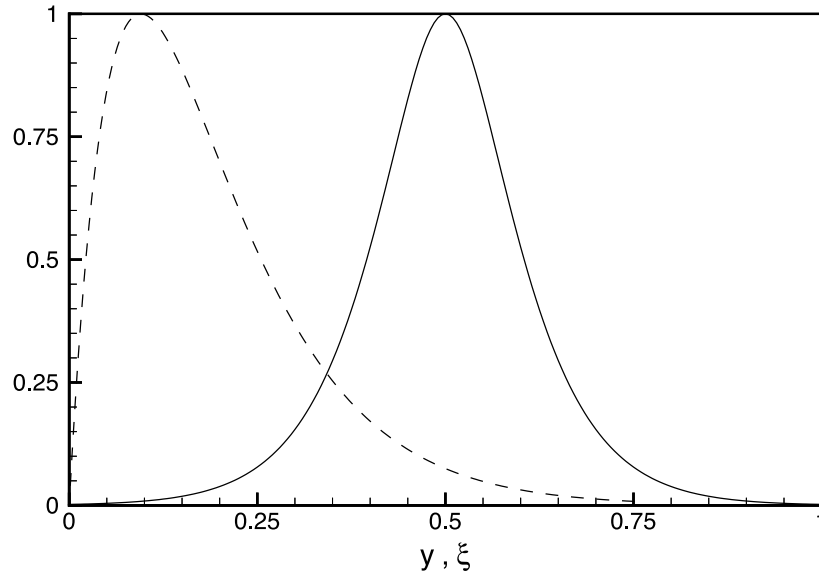


**Figure A2.** Reaction rate functions  $f(y)$  versus  $y$  (broken curve) and  $g(\xi)$  versus  $\xi$  (full curve).  $C = 0.5289$ ,  $B = 0.6684$  and  $\Delta\xi_e = 0.06366$ .

where the scaled variables are

$$\hat{\xi} \equiv \xi/\Delta\xi_e \quad \hat{y} \equiv y/\Delta\xi_e.$$

In a manner analogous to the Lee and Pope thermochemistry [7] take

$$\hat{S}(\hat{\xi}, \hat{y}) = f(\hat{y}) g(\hat{\xi}) \quad (\text{A.9})$$

with

$$f(\hat{y}) = B\hat{y} \exp(1 - B\hat{y}) \quad (\text{A.10})$$

$$g(\hat{\xi}) = \exp[-CG(\hat{\xi})] \quad (\text{A.11})$$

where  $C$  is a constant to be specified, and  $G(\hat{\xi})$ , given by

$$G(\hat{\xi}) = \frac{4}{\pi} \hat{\xi} \arctan(\hat{\xi}) - \frac{2}{\pi} \ln [1 + \hat{\xi}^2] \quad (\text{A.12})$$

is independent of  $\Delta\xi_e$ . Plots of the functions  $f$  and  $g$  are given in figure A2 for the thermochemistry parameters chosen for this study.

#### A.4. Range of applicability of self-similarity

Self-similarity promises access to a much larger range of values of  $\hat{\xi}_r$  than otherwise would be possible, both for PDF methods and for DNS. However, due to the asymptotic nature of various functions used in the definition of this thermochemistry, self-similarity is only maintained accurately for a certain range of parameter values. Specifically, Subramaniam [11] found that accurate self-similarity required that  $\Delta\xi_e \leq 0.0127$ . In DNS it is advantageous to have  $\Delta\xi_e$  as large as possible, since spatial accuracy is directly related to  $\Delta\xi_e$ . By examining the computational cost of satisfying the self-similarity condition on  $\Delta\xi_e$ , using equation (28), it is evident that the cost would be prohibitive at this time. Hence the self-similarity feature of this thermochemistry was not utilized in this work.

## References

- [1] Givi P 1989 Model-free simulation of turbulent reactive flows *Prog. Energy Combust. Sci.* **15** 1–107
- [2] Mahalingam S, Chen J H and Vervisch L 1995 Finite-rate chemistry and transient effects in direct numerical simulations of turbulent nonpremixed flames *Combust. Flame* **102** 285–97
- [3] Montgomery C J, Kosály G and Riley J J 1997 Direct numerical simulation of turbulent nonpremixed combustion with multistep hydrogen–oxygen kinetics *Combust. Flame* **109** 113–44
- [4] Swaminathan N and Bilger R W 1997 Direct numerical simulation of turbulent nonpremixed hydrocarbon reaction zones using a two-step reduced mechanism *Combust. Sci. Technol.* **127** 167–96
- [5] Leonard A D and Hill J C 1991 Scalar dissipation and mixing in turbulent reacting flows *Phys. Fluids A* **3** 1286–99
- [6] Chakrabarti M and Hill J C 1997 First order closure theories for a series-parallel reaction pair in simulated homogeneous turbulence *AIChE J.* **43** 902–12
- [7] Lee Y Y and Pope S B 1995 Nonpremixed turbulent reacting flow near extinction *Combust. Flame* **101** 501–28
- [8] Bilger R W 1980 Turbulent flows with nonpremixed reactants *Turbulent Reacting Flows (Topics in Applied Physics vol 44)* ed P A Libby and F A Williams (Heidelberg: Springer) pp 65–113
- [9] Overholt M R and Pope S B 1998 Numerical investigation of a statistically stationary turbulent reacting flow *Technical Report* no FDA 98-01 Cornell University
- [10] Vervisch L and Poinot T 1998 Direct numerical simulation of non-premixed turbulent flames *Ann. Rev. Fluid Mech.* **30** 655–91
- [11] Subramaniam S 1997 PDF models for mixing in turbulent reactive flows *PhD Thesis* Cornell University
- [12] Ruetsch G R and Maxey M R 1991 Small-scale features of vorticity and passive scalar fields in homogeneous isotropic turbulence *Phys. Fluids A* **3** 1587–97
- [13] Ruetsch G R and Maxey M R 1992 The evolution of small-scale structures in homogeneous isotropic turbulence *Phys. Fluids A* **4** 2747–60
- [14] Holzer M and Siggia E D 1994 Turbulent mixing of a passive scalar *Phys. Fluids* **6** 1820–37
- [15] Pumir A 1994 A numerical study of the mixing of a passive scalar in three-dimensions in the presence of a mean gradient *Phys. Fluids* **6** 2118–32
- [16] Overholt M R and Pope S B 1996 DNS of a passive scalar with imposed mean gradient in isotropic turbulence *Phys. Fluids* **8** 3128–48
- [17] Overholt M R and Pope S B 1998 A deterministic forcing scheme for direct numerical simulations of turbulence *Comput. Fluids* **27** 11–28
- [18] Bilger R W 1993 Conditional moment closure for turbulent reacting flow *Phys. Fluids A* **5** 436–44
- [19] Corrsin S 1952 Heat transfer in isotropic turbulence *J. Appl. Phys.* **23** 113–8
- [20] Sullivan P J 1976 Dispersion of line source in grid turbulence *Phys. Fluids* **19** 159–61
- [21] Durbin P A 1980 A stochastic model of two-particle dispersion and concentration fluctuations in homogeneous turbulence *J. Fluid Mech.* **100** 279–302
- [22] Wiskind H K 1962 A uniform gradient turbulent transport experiment *J. Geophys. Res.* **67** 3033–48
- [23] Alexopoulos C C and Keffer J F 1971 Turbulent wake in a passively stratified field *Phys. Fluids* **14** 216–24
- [24] Venkataramani K S and Chevray R 1978 Statistical features of heat transfer in grid-generated turbulence: constant-gradient case *J. Fluid Mech.* **86** 513–43
- [25] Warhaft Z and Lumley J L 1978 An experimental study of the decay of temperature fluctuations in grid-generated turbulence *J. Fluid Mech.* **88** 659
- [26] Sirivat A and Warhaft Z 1983 The effect of a passive cross-stream temperature gradient on the evolution of temperature variance and heat flux in grid turbulence *J. Fluid Mech.* **128** 323–46
- [27] Jayesh and Warhaft Z 1992 Probability distribution, conditional dissipation and transport of passive temperature fluctuations in grid-generated turbulence *Phys. Fluids A* **4** 2292–307
- [28] Tong C and Warhaft Z 1994 On passive scalar derivative statistics in grid turbulence *Phys. Fluids* **6** 2165–76
- [29] Kerr R M 1985 Higher-order derivative correlations and the alignment of small-scale structures in isotropic numerical turbulence *J. Fluid Mech.* **153** 31–58
- [30] Kerr R M 1990 Velocity, scalar and transfer spectra in numerical turbulence *J. Fluid Mech.* **211** 309–32
- [31] Eswaran V and Pope S B 1988 An examination of forcing in direct numerical simulations of turbulence *Comput. Fluids* **16** 257–78
- [32] Bilger R W, Saetran L R and Krishnamoorthy L V 1991 Reaction in a scalar mixing layer *J. Fluid Mech.* **233** 211–42
- [33] Klimenko A Y 1990 Multicomponent diffusion of various admixtures in turbulent flow *Fluid Dynamics* **25** 327–34
- [34] Bilger R W 1992 Advanced laser diagnostics: implications of recent results for combustor models

- Aerothermodynamics of Combustors* ed R S L Lee, J H Whitelaw and T S Wung (Berlin: Springer) pp 3–16
- [35] Li J D and Bilger R W 1993 Measurement and prediction of the conditional variance in a turbulent reactive scalar mixing layer *Phys. Fluids A* **5** 3255–64
- [36] Mastorakos E and Bilger R W 1998 Second-order conditional moment closure for the auto-ignition of turbulent flows *Phys. Fluids* **10** 1246–48
- [37] Kronenburg A, Bilger R W and Kent J H Second-order conditional moment closure for turbulent jet diffusion flames *27th Int. Symp. on Combustion* (Pittsburgh, PA: Combustion Institute) to appear
- [38] Swaminathan N and Bilger R W Conditional variance equation and its analysis *27th Int. Symp. on Combustion* (Pittsburgh, PA: Combustion Institute) to appear
- [39] Bilger R W 1988 The structure of turbulent nonpremixed flames *22nd Int. Symp. on Combustion* (Pittsburgh, PA: Combustion Institute) pp 475–88
- [40] Rogallo R S 1981 Numerical experiments in homogeneous turbulence *Technical Report* no 81315, NASA Tech. Mem.
- [41] Pope S B 1990 Computations of turbulent combustion: progress and challenges *23rd Int. Symp. on Combustion* (Pittsburgh, PA: Combustion Institute) pp 591–612
- [42] Fox R O 1997 The Lagrangian spectral relaxation model of the scalar dissipation in homogeneous turbulence *Phys. Fluids* **9** 2364–86